Sequential star formation in the filamentary structures of the *Planck* Galactic cold clump G181.84+0.31

Lixia Yuan [1,2,3]★ Ming Zhu,[1,3]★ Tie Liu,[4,5] Jinghua Yuan,[1] Yuefang Wu,[6] Kee-Tae Kim,[4] Ke Wang,[7,8] Chenlin Zhou [1,2,3] Ken'ichi Tatematsu [9] and Nario Kuno[10,11]

[1]*National Astronomical Observatories, Chinese Academy of Sciences, 20A Datun Road, Chaoyang District, Beijing 100101, China*
[2]*University of Chinese Academy of Sciences, 100049, Beijing, China*
[3]*Key Laboratory of FAST, NAOC, Chinese Academy of Sciences, Beijing 100012, China*
[4]*Korea Astronomy and Space Science Institute, 776 Daedeokdae-ro, Yuseong-gu, Daejeon 34055, Republic of Korea*
[5]*East Asian Observatory, 660 N. A'ohoku Place, Hilo, HI 96720, USA*
[6]*Department of Astronomy, Peking University, 100871, Beijing China*
[7]*Kavli Institute for Astronomy and Astrophysics, Peking University, 5 Yiheyuan Road, Haidian District, Beijing 100871, China*
[8]*European Southern Observatory (ESO) Headquarters, Karl-Schwarzschild-Str. 2, 85748 Garching bei München, Germany*
[9]*National Astronomical Observatory of Japan, 2-21-1 Osawa, Mitaka, Tokyo 181-8588, Japan*
[10]*Tomonaga Center for the History of the Universe, University of Tsukuba, 1-1-1 Tennodai, Tsukuba, Ibaraki 305-8571, Japan*
[11]*Department of Physics, Graduate School of Pure and Applied Sciences, University of Tsukuba, 1-1-1 Ten-nodai, tsukuba, Ibaraki 305-8577, Japan*

ABSTRACT

We present a multiwavelength study of the *Planck* Galactic cold clump G181.84+0.31, which is located at the northern end of the extended filamentary structure S242. We have extracted nine compact dense cores from the SCUBA-2 850-μm map, and we have identified 18 young stellar objects (YSOs; four Class I and 14 Class II) based on their *Spitzer*, *Wide-field Infrared Survey Explorer* (*WISE*) and Two-Micron All-Sky Survey (2MASS) near- and mid-infrared colours. The dense cores and YSOs are mainly distributed along the filamentary structures of G181.84 and are well traced by $HCO^+(1–0)$ and $N_2H^+(1–0)$ spectral-line emission. We find signatures of sequential star formation activities in G181.84: dense cores and YSOs located in the northern and southern substructures are younger than those in the central region. We also detect global velocity gradients of about 0.8 ± 0.05 and 1.0 ± 0.05 km s^{-1} pc^{-1} along the northern and southern substructures, respectively, and local velocity gradients of 1.2 ± 0.1 km s^{-1} pc^{-1} in the central substructure. These results might be due to the fact that the global collapse of the extended filamentary structure S242 is driven by an edge effect, for which the filament edges collapse first and then further trigger star formation activities inward. We identify three substructures in G181.84 and estimate their critical masses per unit length, which are $\sim 101 \pm 15$, 56 ± 8 and 28 ± 4 M$_\odot$ pc^{-1}, respectively. These values are all lower than the observed values (~ 200 M$_\odot$ pc^{-1}), suggesting that these substructures are gravitationally unstable.

Key words: stars: formation – stars: protostars – ISM: clouds – ISM: kinematics and dynamics – ISM: structure.

1 INTRODUCTION

Recent dust continuum surveys, such as the APEX Telescope Large Area Survey of the Galaxy (ATLASGAL; Schuller et al. 2009), the Bolocam Galactic Plane Survey (BGPS; Nordhaus et al. 2008) and the *Herschel* infrared Galactic Plane Survey (Hi-GAL; Molinari et al. 2010), have revealed that filamentary structures are ubiquitous along the Galactic plane. Wang et al. (2015, 2016) have identified 56 large-scale, velocity-coherent, dense filaments throughout the Galaxy, which is the first comprehensive catalogue of large filaments. Li, Klein & McKee (2016) also identified ∼517 filamentary structures in the inner Galaxy. These filamentary structures are tightly correlated with the spiral arms and have a

broad range of lengths and a variety of aspect ratios, widths and masses (Li et al. 2016; Hacar et al. 2018; Arzoumanian et al. 2019). In addition, studies based on *Herschel* data, and other observations (e.g. near-infrared extinction), have found that more than 70 per cent of gravitationally bound dense cores and protostars are embedded in filaments that are supercritical (Schneider et al. 2012; André et al. 2013, 2014; Contreras et al. 2016; Li et al. 2016). There is a general consensus that large-scale supersonic flows compress the gas, driving the formation of filaments in the cold interstellar medium, and then the filaments gravitationally fragment into pre-stellar cores and ultimately form protostars (André et al. 2013; André 2017).

Pon, Johnstone & Heitsch (2011) and Pon et al. (2012) found that global collapse in filamentary geometry (especially for those with aspect ratio $A_o \gtrsim 5.0$) tends to be influenced by an edge effect, such as end-dominated collapse. Their ends are preferentially accelerated, and further locally collapse in density enhancement to form stars. Johnstone et al. (2017) found a variation in evolutionary ages between the two end-regions of IC 5146. However, high-resolution observations with the Atacama Large Millimeter/submillimeter Array (ALMA) also reveal that edge instabilities can also affect the separation of the condensations in the edge-regions of filaments or pre-stellar cores (Kainulainen et al. 2017; Ohashi et al. 2018). Therefore, edge acceleration might play a role in the formation of protostars in filaments.

S242 is an elongated filamentary structure (EFS) with a length of ∼25 pc and a velocity ranging from –3 to 5 km s^{-1} (Dewangan et al. 2017). The two end-regions of this filament contain most of the massive clumps and YSO clusters. Such a distribution is consistent with the prediction of the end-dominated collapse scenario for star formation in filamentary clouds (Dewangan et al. 2017). The southern end of S242 is associated with an H II region, ionized by the star BD+26 980 with a spectral type of B0V (Hunter & Massey 1990). The temperatures near the ionized gases and warm dusts can be up to ∼30 K, while the northern end is coincident with the *Planck* Galactic cold clump (PGCC) G181.84+0.31 (hereafter referred to as G181), which has a column density of ∼10^{22} cm^{-2} and relatively low dust temperatures of 10–12 K. G181 is located at a kinematic distance of 1.76 ± 0.04 kpc, which was estimated using the parallax-based distance estimator for spiral arm sources (Reid et al. 2016).

In order to investigate the role of edge instabilities in star formation in gas filaments, we have made detailed analyses of the star formation activities and dense gas distribution at the northern end of S242 (G181); this end is not influenced by the circumambient environment. Furthermore, PGCCs typically have significant substructures and are often associated with cloud filaments (Rivera-Ingraham et al. 2016). Follow-up observations in molecular lines and dust continuum emission have already resolved dense filaments inside some PGCCs (Kim et al. 2017; Liu et al. 2018a,b; Zhang et al. 2018). G181 was first detected by Ade et al. (2011). We divided the G181 region into three parts, as outlined by the cyan-dashed boxes of the upper-left panel in Fig. 1: Fa for the central substructure, and Fb and Fc for the northern and southern substructures, respectively. Note that a far-infrared source, IRAS 05483+2728, is embedded in the Fa substructure.

The paper is organized as follows. In Section 2, we present the observations and data reductions. In Section 3, we present the results. In Section 4, we discuss the relationship between filaments and star formation. We present the conclusions of this study in Section 5.

2 OBSERVATIONS AND DATA REDUCTION

2.1 Continuum emission

2.1.1 The SCUBA-2 observations

The 850-μm continuum observations of G181 were carried out with the James Clerk Maxwell Telescope (JCMT)[1] in 2015 September. This source was included in the SCUBA-2 Continuum Observations of Pre-protostellar Evolution (SCOPE[2]) large project, which aims to study the roles of filaments in dense core formation and to investigate dust properties and detect rare populations of dense clumps (Liu et al. 2016a, 2018a; Eden et al. 2019). The observations were conducted using the CV Daisy mode. The CV Daisy provided a deep 3-arcmin (in diameter) region in the centre of the map, but covered out to beyond 12 arcmin (Bintley et al. 2014). We took a mean flux conversion factor (FCF) of 554 Jy pW^{-1} beam^{-1} to convert data from pW to Jy beam^{-1}. The beam size at 850 μm is ∼14 arcsec and the main-beam efficiency is about 0.85. The observations were carried out under grade 3/4 weather conditions. The 225-GHz opacity was between 0.1 and 0.15. The rms noise level of the map is ∼6–10 mJy beam^{-1} in the central 3-arcmin region, and increases to 10–30 mJy beam^{-1} out to the 12-arcmin area. This sensitivity is better than the value of 50–70 mJy beam^{-1} in the ATLASGAL (Contreras et al. 2013).

2.1.2 Herschel and WISE archive data

We also use the level 3.0 SPIRE maps and level 2.5 PACS maps available in the *Herschel* Science Archive. The observations for SPIRE (250–500 μm band) and PACS (70- and 160-μm bands) maps were carried out in parallel mode with fast scanning speed (60 arcsec s^{-1}). The FWHM beam sizes of the original *Herschel* maps are approximately 9.2, 12.3, 17.6, 23.9 and 35.2 arcsec at 70, 160, 250, 350 and 500 μm, respectively.

The *Wide-field Infrared Survey Explorer* (*WISE*) surveyed the entire sky in four mid-infrared bands (3.4, 4.6, 12 and 22 μm). The angular resolutions of the *WISE* maps are respectively 6.1, 6.4, 6.5 and 12.0 arcsec at the corresponding *WISE* bands. We retrieved the processed *WISE* images and catalogue data via the NASA/IPAC Infrared Science Archive (IRSA). The 5σ point source sensitivities in the AllWISE catalogue are respectively better than 0.08, 0.11, 1 and 6 mJy in unconfused regions at the corresponding *WISE* bands. The position precision for high signal-to-noise (S/N) sources is better than 0.15 arcsec (Wright et al. 2010).

2.2 Spectral-line emission

2.2.1 Observations with the Nobeyama 45-m telescope

We have carried out on-the-fly (OTF) mapping observations for the G181 structures in the $J = 1–0$ transition lines of HCO$^+$

---

[1]The JCMT is the largest single-dish astronomical telescope in the world with a diameter of 15 m designed specifically to operate in the submillimetre wavelength. SCUBA-2 (the Submillimeter Common-User Bolometer Array) is bolometer operating simultaneously at 450 and 850 μm with an innovative 10 000 pixel bolometer camera (Holland et al. 2013).
[2]https://www.eaobservatory.org/jcmt/science/large-programs/%20scope/
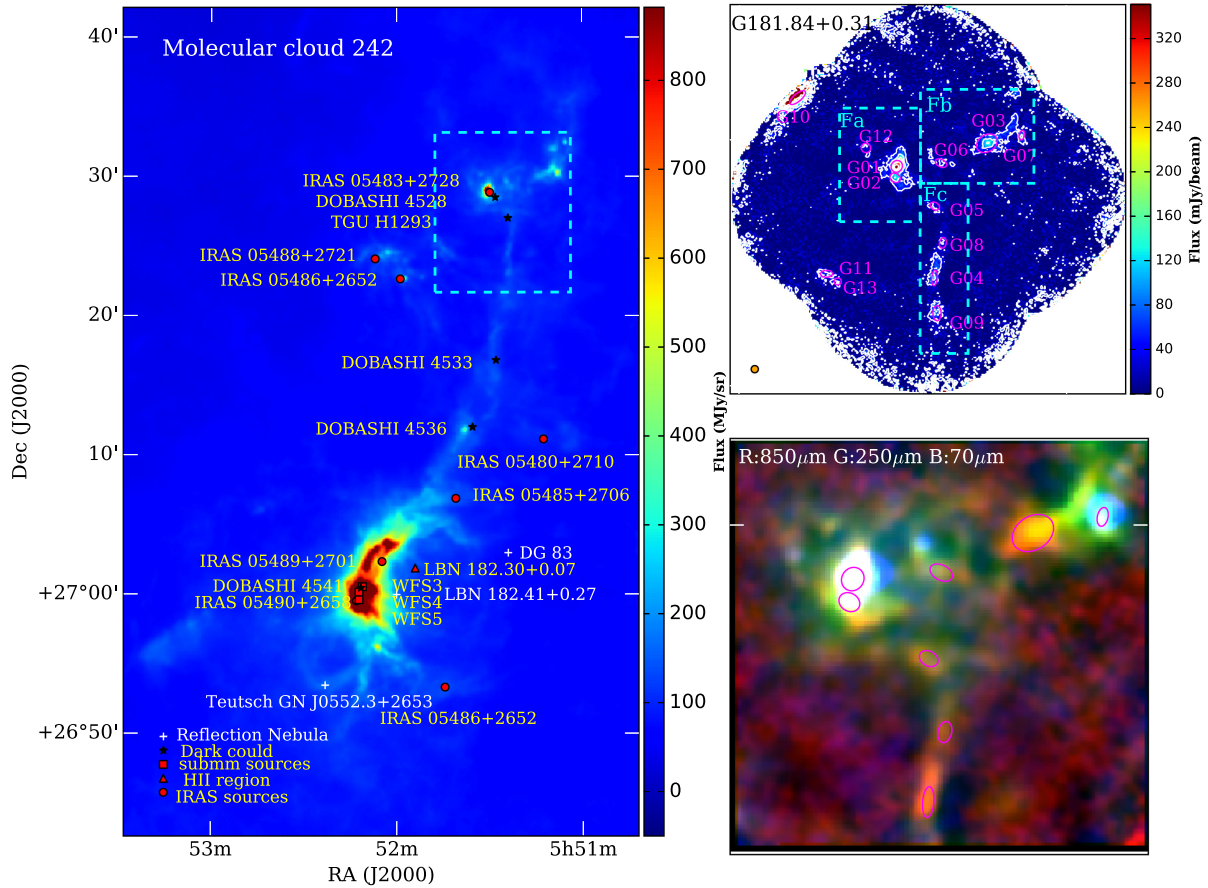
Figure 1. In the left panel, the S242 molecular cloud is an EFS with a length of ∼25 pc (Dewangan et al. 2017). The red circle, triangle and square denote the IRAS sources, H II region and submm sources, respectively, and the black stars and white crosses represent dark clouds and white reflection nebula. All of these have been retrieved from the SIMBAD astronomical database. The PGCC G181.84 region is outlined by the cyan-dashed box. The upper-right panel shows the SCUBA-2 850-μm continuum emission map for PGCC G181.84+0.31 with contour levels from 10 to 90 per cent by step intervals of 15 per cent of the peak value (350 mJy beam^{-1}). Magenta ellipses denote the compact sources extracted from the 850-μm map. The orange circle in the right corner shows the SCUBA-2 effective beam size for SCUBA-2 at 850 μm. The cyan-dashed boxes labelled Fa, Fb and Fc represent three major emission substructures in G181. The lower right panel shows a three-colour map for G181, made using the SCUBA-2 850-μm in red, SPIRE 250-μm in green and PACS 70-μm in blue.

and N$_2$H$^+$ using the Nobeyama Radio Observatory (NRO)[3] 45-m telescope in 2018 January. We used the four-beam receiver (FOREST) with the Spectral SAM45 backend, which processes 16 IFs simultaneously. We used IF-A to cover the HCO$^+$(1–0) line with a spectral bandwidth of 125 MHz centring at the rest frequency of 89.19 GHz, and the IF-B to cover the N$_2$H$^+$(1–0) line with the same bandwidth centring at the rest frequency of 93.17 GHz. The FWHM beam sizes (θ_{HPBW}) are ∼18.9 ± 0.5 arcsec and 19.2 ± 0.6 arcsec at 86 GHz in H and V polarizations, respectively. The main beam efficiencies (η_{mb}) are 55 ± 5 and 58 ± 5 per cent at 86 GHz in H and V polarizations, respectively. The OTF mapping was performed for three areas (300 × 220, 190 × 135 and 240 × 110 arcsec^2) covering the whole G181 region. An rms noise level of ∼0.1 K (T_{mb}) was achieved by co-adding all the observed maps. The telescope pointing was checked about every 1.2 h, and the accuracy was within 3 arcsec. The data were reduced using the software package NOSTAR[4] of the NRO. By using a spheroidal function as a griding convolution

function, we produced a data cube with a grid spacing of 6 arcsec and a velocity resolution of 0.2 km s^{-1}.

Furthermore, we have also performed single-point observations of the H^{13}CO$^+$(1–0) line toward the G01–G03 cores with the T70 receiver in position switching mode. The beam size of the T70 receiver at this line frequency was 19 arcsec and η_{mb} was 55 per cent. The velocity resolution was 0.13 km s^{-1} and an rms noise level of 0.03 K (T_{mb}) was achieved.

2.2.2 ^{12}CO(1–0), ^{13}CO(1–0) spectral lines from the Purple Mountain Observatory

The mapping data of G181 in ^{12}CO(1–0) and ^{13}CO(1–0) were extracted from the CO line survey for the PGCCs using the 13.7-m telescope of the Purple Mountain Observatory (PMO) by Wu et al. (2012). The half-power beamwidth at 115 GHz is 52 ± 3 arcsec. The main beam efficiency is about 50 per cent. The typical system temperature (T_{sys}) is about 110 K and varies by ∼10 per cent for each beam. The velocity resolution is 0.16 km s^{-1} for the ^{12}CO(1–0) line and 0.17 km s^{-1} for the ^{13}CO(1–0) line. An rms noise level of 0.2 K in T_A^* for the ^{12}CO(1–0), and 0.1 K for the ^{13}CO(1–0) line was achieved. The mapped region has a size of 22 × 22 arcmin^2 centring

at the PGCC G181. The scanning speed was 20 arcsec s^{-1}. The noisy edges of the OTF maps were cropped, and only the central 14 × 14 arcmin^2 regions were kept for further analyses. The cube data were calibrated in GILDAS and gridded with a spacing of 30 arcsec (Liu, Wu & Zhang 2012; Wu et al. 2012; Meng, Wu & Liu 2013).

3 RESULTS

3.1 Pixel-to-pixel spectral energy distribution fitting

3.1.1 Convolution to a common resolution and foreground/background filtering

We use the multiwavelength continuum maps to estimate the physical properties of G181. First, the images of different wavelength bands were cropped to the same size, and transferred to the same unit for the value in every pixel. Then, we re-gridded maps to let them align with each other pixel-by-pixel with a common pixel size of 14 arcsec using the imregrid algorithm of CASA.[5]

The maps were convolved with Gaussian kernels to obtain images with an angular resolution of 35.2 arcsec, which matches the resolution of the un-convolved *Herschel* 500-μm map (whose angular resolution is the lowest). We used the convolution package of ASTROPY (Robitaille et al. 2013) with a Gaussian kernel of

$$\sqrt{35.2^2 - \theta_\lambda^2},\tag{1}$$

where θ_λ is the FWHM beam size for the corresponding *Herschel* or SCUBA-2 bands.

In order to reduce the atmospheric emission, the uniform astronomical signals in the SCUBA-2 images beyond the spatial scales of 200 arcsec have been filtered out. Following Yuan et al. (2017), we iteratively filtered the *Herschel* images using the CUPID-findback algorithm of the Starlink[6] suite, which was developed for the SCUBA-2 data reduction. Further details of the algorithm are available in the online documentation for findback.[7]

3.1.2 Spectral energy distribution fitting

We used the smoothed and background-removed far-infrared to submillimetre band maps, including *Herschel* (160–500 μm) data and SCUBA-2 850-μm data, to fit the intensity as a function of wavelength for each pixel through the modified blackbody model,

$$I_\nu = B_\nu(T)(1 - e^{-\tau_\nu}),\tag{2}$$

where the *Planck* function $B_\nu(T)$ is modified by the optical depth:

$$\tau_\nu = \mu_{H_2} m_H \kappa_\nu N_{H_2} / R_{gd}.\tag{3}$$

Here, μ_{H_2} = 2.8 is the mean molecular weight (Kauffmann et al. 2008), m_H is the mass of a hydrogen atom, R_{gd} = 100 is the gas-to-dust ratio and N_{H_2} is the H$_2$ column density. The dust opacity κ_ν can be expressed as a power law in frequency,

$$\kappa_\nu = 3.33 \left(\frac{\nu}{600 \, \text{GHz}}\right)^\beta \, \text{cm}^2 \, \text{g}^{-1},\tag{4}$$

where κ_ν (600 GHz) is the dust opacity, listed in table 1 of Ossenkopf & Henning (1994), but the value has been scaled down a factor of 1.5 as suggested in Kauffmann et al. (2010). We took the

dust emissivity index β as 2.0, which is the standard value for cold dust emission (Hildebrand 1983).

The fitting was performed using the algorithm in the PYTHON package scipy.optimize.[8] For each pixel, only the data with S/N > 3 were included to perform the fitting. We considered flux uncertainties of the order of ∼15 per cent in all *Herschel* images, based on the work previously reported by Launhardt et al. (2013).

The maps of H$_2$ column density (N_{H_2}) and dust temperature (T_d) are presented in Fig. 2. The N_{H_2} values across the filamentary structures are mainly around 1.0×10^{22} to 4.0×10^{22} cm^{-2} and the range of T_d is from 8 to 16 K. A single-temperature greybody model can fit the cold dust emission well, but cannot account for the 70-μm emission, because the 70-μm flux is mostly from the warm dust surrounding protostars. Therefore, we did not take the 70-μm data into account for the spectral energy distribution (SED) fitting. It should be noted that the dust temperatures could be underestimated, especially for substructure Fa whose 70-μm dust emission is relatively strong. Moreover, the dust opacity, which is subject to a factor of 2 uncertainties (Ossenkopf & Henning 1994), can induce uncertainties in N_{H_2} and T_d. The dust emissivity index (β) can also significantly influence the derived results. If β increases or decreases by 50 per cent, the resultant N_{H_2} will increase by 2–35 per cent, or decrease by 10–35 per cent, while T_d could have a 5–18 per cent decrease or a 13–28 per cent increase, respectively (Yuan et al. 2017).

Additionally, we estimated the effects of the filtering processes on the results of our SED fitting. For the substructures Fb and Fc, the H$_2$ column densities derived from unfiltered maps increase by 30–50 per cent, when compared with the values derived from the filtered maps. However, we found that the background filter has little effect on the derived H$_2$ column densities in substructure Fa.

From the N_{H_2} map in Fig. 2, we find that there are dense clumps and fragments unevenly distributed along the structures. Based on the overlaid contours on the temperature map in the right panel of Fig. 2, we see that the Fb and Fc filamentary substructures presented relatively lower dust temperatures. The west part of Fb showing higher temperatures seems to compress the ambient matter, while substructure Fa has higher dust temperatures, which might be heated by the formed protostars.

Dewangan et al. (2017) have published the H$_2$ column density and dust temperature maps of the molecular cloud S242. The H$_2$ column density in G181 is about $(0.6-1.5) \times 10^{22}$ cm^{-2}, approximately 50 per cent less than the results of our fitting, $(1.0-4.0) \times 10^{22}$ cm^{-2}. The dust temperature distribution of G181 derived by Dewangan et al. (2017) is about 9–14 K, while our result is about 7–16 K. Such a difference might be due to the fact that the 850-μm flux is sensitive to cold dust emission and can better constrain the SED than using *Herschel* data alone.

Under the assumption of local thermal equilibrium (LTE), we further derived the H$_2$ column density maps using the ^{12}CO(1–0) and ^{13}CO(1–0) spectral lines from the PMO through equations (4)–(13) in Qian, Li & Goldsmith (2012). As presented in Fig. A1, the CO excitation temperatures range from 8 to 14 K. The ^{13}CO column density is distributed in the range of $0.6-1.4 \times 10^{16}$ cm^{-2}. Using an abundance ratio of ^{13}CO and H$_2$ ([^{13}CO]/[H$_2$]) of 1.7×10^{-6} (Frerking, Langer & Wilson 1982), the derived H$_2$ column density ranges between 1.0×10^{22} and 2.4×10^{22} cm^{-2}, which is a factor of 1.5 higher than the N_{H_2} range from Dewangan et al. (2017), 0.6–

---

[5] https://casa.nrao.edu/docs/TaskRef/imregrid-task.html
[6] http://starlink.eao.hawaii.edu/starlink/WelcomePage/
[7] http://starlink.eao.hawaii.edu/starlink/findback.html/

[8] https://docs.scipy.org/doc/scipy/reference/generated/scipy.optimize.curve_fit.html#scipy.optimize.curve_fit
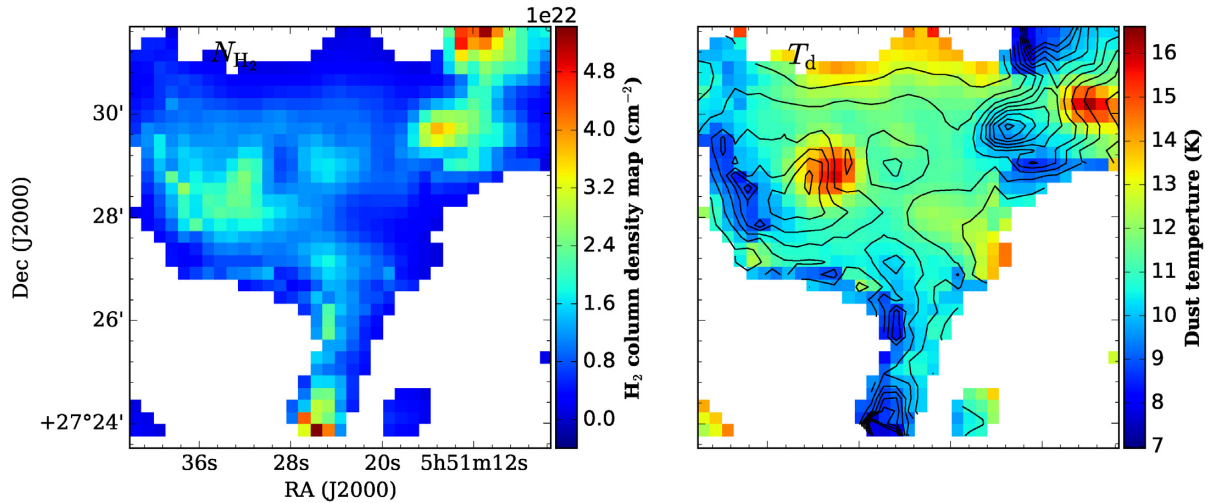
Figure 2. Left panel: H_2 column density map. Right panel: dust temperature map. Both N_{H_2} and T_d are obtained from the SED fitting based on the greybody radiation mode using *Herschel* (160–500 μm) and SCUBA-2 850-μm photometric data. The black contours show the H_2 column density with levels stepped from 0.1 to 0.9 by 0.1 multiplied by the peak value of 4.0×10^{22} cm^{-2}.

1.5×10^{22} cm^{-2}. This further confirms that the H_2 column density derived by SED fitting using only the *Herschel* data (160–500 μm) might be underestimated.

3.2 Dense cores

3.2.1 Identification of compact sources

We have used the FellWalker[9] (Berry 2015) source-extraction algorithm to identify compact sources from the 850-μm continuum image. We follow the source-extraction processes used by the JCMT Plane Survey and detailed descriptions are given in Moore et al. (2015) and Eden et al. (2017).

We set a detection threshold of 3σ and constructed a mask in the S/N map. The extracted sources were required to consist of at least seven continuous pixels. A total of 13 compact sources have been extracted, called G01–G13. Table 1 lists the coordinates, size, peak flux density and integrated flux density at 850 μm. The identified compact sources are shown as magenta ellipses in the upper-right panel of Fig. 1. We manually rejected sources not associated with the filamentary structures of G181. Finally, a total of nine compact sources, G01–G09, were included in our further analysis (see Table 2).

3.2.2 The properties of compact sources

For each core, we calculated the flux in a convolved size at *Herschel* (160–500 μm) and SCUBA-2 (850 μm) bands. The uncertainties of the flux values are estimated from the background noise of different wavelength images. We derived the dust temperature (T_d), column density (N_{H_2}), volume density (n_{H_2}), core masses (M_c) based on the modified blackbody model (equations 2, 3 and 4). The effective radius is defined as $R_{eff} = \sqrt{ab}$, where a and b are

[9]FellWalker is included the Starlink software package CUPID (Berry et al. 2007). The FellWalker algorithm extracts compact sources by following the steepest gradients to reach a significant summit.

the core semimajor/minor axes. The volume number density (n_{H_2}) and column density (N_{H_2}) are derived as

$$n \times \left(\frac{4}{3}\pi R_{eff}^3 \mu m_H \right) = N \times (\pi R_{eff}^2 \mu m_H) = M_c,$$

where $\mu = 2.8$ is the mean molecular weight per H and m_H is the atomic hydrogen mass. The fitted results are presented in Fig. 3. For sources with 70-μm fluxes that obviously deviate from the SED fitting, we exclude these data points in our fitting.

As shown in the lower-right panel of Fig. 1, we composed a three-colour image with the 850-, 250- and 70-μm band images, respectively, displayed as red, green and blue colours. Because the 70-μm emission is dominated by the ultraviolet (UV) heated warm dust, it can trace very well the internal luminosity of a protostar (Dunham et al. 2008). From the three-colour image of Fig. 1 and the SED fitting plots of Fig. 3, we can see that only G01, G02, G07 and G09 have 70-μm emission (i.e. a sign of protostellar activity). There is no (or faint) 70-μm emission in the dense cores G03, G04, G05, G06 and G08, so these cores could be pre-stellar candidates. Recent works have shown that infall signatures have been found in some of the massive 70-μm quiet clumps and pre-stellar cores, which provide evidence for embedded low/intermediate-mass star formation activity (Traficante et al. 2017; Liu et al. 2018b; Contreras et al. 2018).

3.2.3 Source characteristics from spectral-line data

We used the average intensity of the N_2H^+ and HCO^+(1–0) lines in each core, and further fitted the emission using PYSPECKIT (Ginsburg & Mirocha 2011). The dense core G09 was not covered by our line observations, and G08 was not fitted due to the low S/N ratio of the N_2H^+ emission. The fitted spectra are shown in Figs A3 and A4. The line parameters for the N_2H^+(1–0) model are based on the analysis of Daniel et al. (2005) and Schöier et al. (2005). The derived parameters include the optical depth, excitation temperature, centroid velocity and velocity dispersion. A Gaussian model was used to fit the HCO^+(1–0) line to derive the peak intensity, centroid velocity and velocity dispersion. All these derived parameters are listed in Table 3.

Table 1. The extracted compact sources from the SCUBA-2 map in PGCC G181.84.

Source name	RA$_{peak}$ (hh:mm:ss)	Dec.$_{peak}$ (dd:mm:ss)	RA$_{cen}$ (hh:mm:ss)	Dec.$_{cen}$ (dd:mm:ss)	σ_{maj} (arcsec)	σ_{min} (arcsec)	PA (degree)	S_{int} (Jy)	S_{peak} (mJy beam^{-1})
G01	5:51:31.2	27:28:54.48	5:51:31.20	27:29:00.19	13.3	14.7	296.6	1.6(0.25)	360.9
G02	5:51:31.5	27:28:26.4	5:51:30.46	27:28:18.6	13.3	10.9	253.4	0.46(0.15)	143.0
G03	5:51:14.7	27:29:50.64	5:51:13.1	27:30:00	27.1	20.3	302.2	1.24(0.19)	146.7
G04	5:51:24.29	27:24:22.68	5:51:24.09	27:24:42.68	6.8	18.8	347.6	0.47(0.12)	126.4
G05	5:51:25.5	27:27:18.36	5:51:24.2	27:27:18.0	12.1	8.9	240.6	0.15(0.04)	49.5
G06	5:51:23.09	27:29:02.40	5:51:23.7	27:29:09.8	14.7	9.2	243.6	0.21(0.04)	52.8
G07	5:51:08.4	27:30:07.2	5:51:08.30	27:30:10.25	6.4	11.6	347.7	0.16(0.05)	113
G08	5:51:23.09	27:25:54.48	5:51:22.76	+27:25:48.02	8.3	13	346.9	0.12(0.02)	55.8
G09	5:51:24.3	27:23:06.4	5:51:23.83	+27:22:57.06	10	18.3	180.6	0.37(0.04)	102.4
G10	5:51:49.56	27:31:50.52	5:51:49.37	+27:31:41.75	23.8	9.3	309.9	3.2(0.25)	618.5
G11	5:51:45.34	27:24:34.56	5:51:44.040	+27:24:32.78	14.7	8.4	272.05	0.18(0.03)	73.3
G12	5:51:36.62	27:29:18.6	5:51:36.85	+27:29:39.36	11.6	11.3	229.4	0.14(0.03)	49.4
G13	5:51:41.7	27:24:06.5	5:51:42.00	+27:24:14.06	8.7	8.3	305.5	0.1(0.03)	56.2
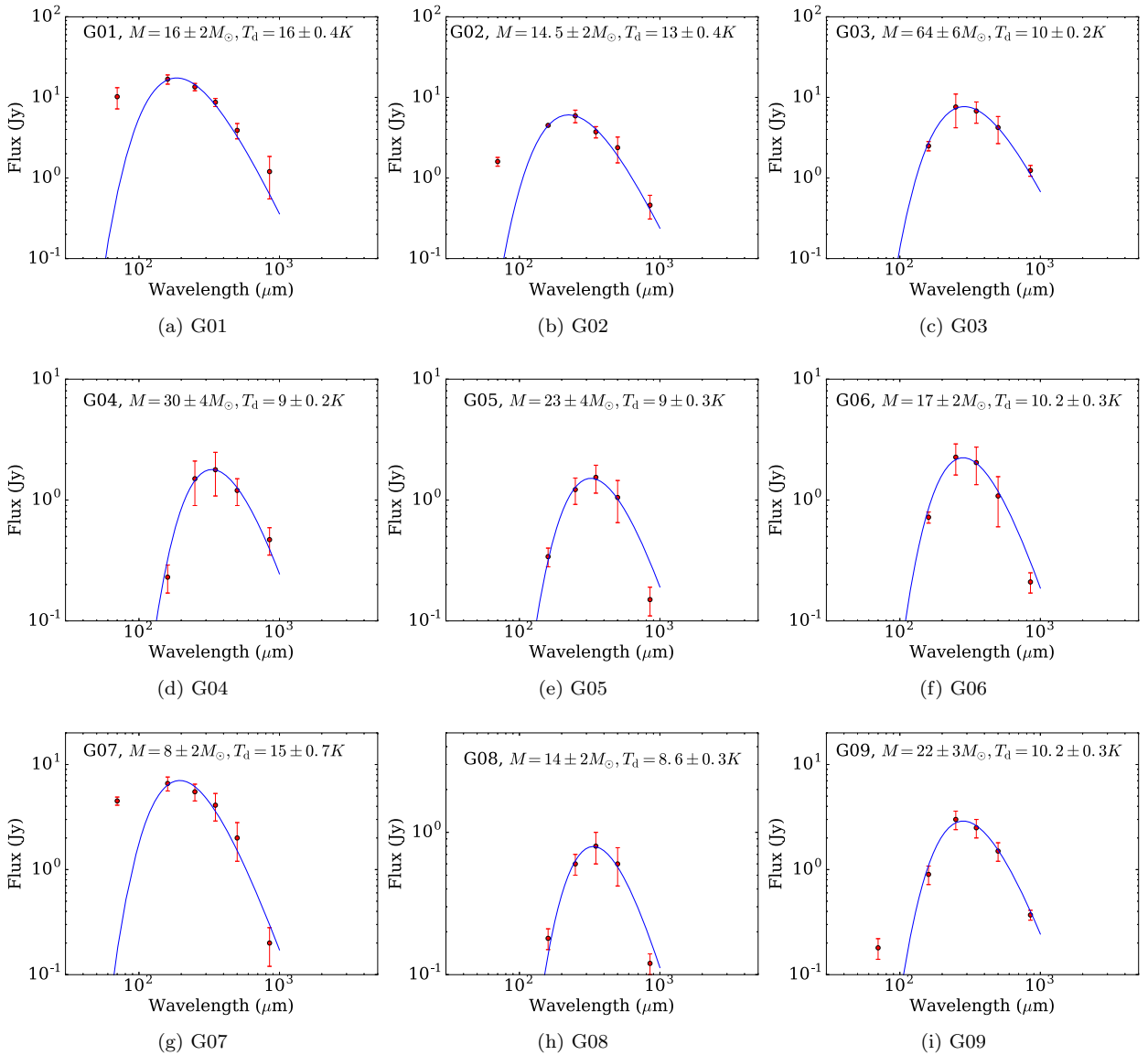
Figure 3. The SED fitting for compact sources in G181 with *Herschel* (160–500 μm) and SCUBA-2 (850 μm) photometrics, based on the modified blackbody model.

Table 2. Parameters of the compact sources.

Source name	RA (hh:mm:ss)	Dec. (dd:mm:ss)	$R_{\rm eff}$ (pc)	$T_{\rm d}$ (K)	$N_{\rm H_2}$ (10^{22} cm^{-2})	$n_{\rm H_2}$ (10^5 cm^{-3})	$M_{\rm c}$ (M$_\odot$)	Luminosity (L$_\odot$)
G01	5:51:30.960	27:28:59.92	0.12	16(0.4)	1.6(0.2)	4.3	16(2)	31.6
G02	5:51:30.542	27:28:19.81	0.1	13(0.4)	1.9(0.3)	6.1	14.5(2)	9
G03	5:51:13.826	27:29:57.55	0.2	10(0.2)	2.3(0.3)	3.7	64(6)	9
G04	5:51:24.091	27:24:43.96	0.1	9(0.2)	4.6(0.15)	15.7	30(4)	1.8
G05	5:51:24.233	27:27:17.80	0.09	9(0.3)	4.1(0.6)	15.0	23(3)	1.6
G06	5:51:23.748	27:29:09.53	0.1	10.2(0.3)	2.5(0.5)	8.0	17(2)	2.7
G07	5:51:08.30	27:30:10.25	0.07	15(0.7)	2.2(0.3)	9.7	8(2)	12
G08	5:51:22.76	+27:25:48.02	0.09	8.6(0.3)	2.6(0.4)	9.5	14(2)	0.8
G09	5:51:23.83	+27:22:57.06	0.1	10.2(0.3)	2.4(0.5)	6.7	22(3)	3.4

Table 3. The parameters of compact sources from spectral lines.

Source name	$V_{\rm lsr}$ (km s^{-1})	τ	Excitation temperature (K)	$\sigma_{\rm N_2H^+}$ (km s^{-1})	$\sigma_{\rm HCO^+}$ (km s^{-1})	Mass$_{\rm vir}$ (M$_\odot$)	α
G01	2.4(0.01)	2.12(0.61)	7.9(1.1)	0.408(0.016)	0.866(0.021)	14(1.2)	0.9(0.1)
G02	2.28(0.022)	1(1)	6.7(2.7)	0.402(0.027)	1.18(0.03)	11.3(1.6)	0.8(0.1)
G03	2.9(0.008)	3.83(0.96)	4.33(0.26)	0.236(0.008)	0.482(0.011)	7.8(0.53)	0.12(0.01)
G04	1.14(0.01)	4.7(1.1)	5.03(0.32)	0.243(0.01)	0.432(0.017)	4.1(0.34)	0.14(0.02)
G05	1.7(0.05)	2.3(1.7)	3.63(0.45)	0.52(0.066)	0.608(0.031)	17.0(4.3)	0.4(0.03)
G06	1.89(0.01)	2.3(1.2)	6.0(1.3)	0.255(0.012)	0.44(0.01)	3.6(0.4)	0.2(0.03)
G07	2.68(0.031)	3.6(1.4)	3.9(0.25)	0.453(0.04)	0.75(0.02)	10(2)	0.8(0.2)

We found that the velocity dispersions derived from the HCO$^+$(1–0) line are about two times larger than the values from N$_2$H$^+$(1–0). This might be because the N$_2$H$^+$ emission, a well-known dense gas tracer for the cold dense cores, is closely associated with the densest parts of cores (Caselli et al. 2002). Besides, N$_2$H$^+$ can well trace the central region with CO depletion (Bergin et al. 2001, 2002) and less affected by star formation activities, such as molecular outflows (Womack, Ziurys & Sage 1993). While HCO$^+$ emission, which is produced by the protonation of CO, is not abundant at the core centre and might be more optically thick (di Francesco et al. 2007). Therefore, we used the velocity dispersion derived from the N$_2$H$^+$(1–0) line to compute the virial mass of each core. The virial mass is computed with the following equation mentioned in MacLaren, Richardson & Wolfendale (1988) and Williams (1994):

$$M_{\rm vir} = 3k \frac{r \times \sigma_\upsilon^2}{G}.$$

Here, G is the gravitational constant, r is the radius for each core, σ_υ represents the line-of-sight velocity dispersion and $k = (5 - 2a)/(3 - a)$ is a correction factor corresponding to the density profile $\rho \propto r^{-a}$. Assuming that the dense cores are gravitationally bound isothermal spheres, with a density profile of $\rho \sim r^{-2}$ ($a = 2$), the above equation could be rewritten as

$$M_{\rm vir} = 126 \left(\frac{r}{\rm pc}\right) \left(\frac{\Delta V_{\rm FWHM}}{\rm km\ s^{-1}}\right)^2 {\rm M}_\odot.$$

Here, $\Delta V_{\rm FWHM}$ is the FWHM of the N$_2$H$^+$ line along the line of sight. The resultant virial mass for each core is listed in Table 3. In addition, we derived the virial parameters (α, $M_{\rm vir}/M_{\rm c}$) for each core. Most of our dense cores have low virial parameters ($\alpha \ll 2$), which are consistent with those observed in high-mass star-forming regions (Kauffmann, Pillai & Goldsmith 2013), suggesting rapid and violent collapse or magnetic field support. However, it should be noted that there could be a bias in the measurement of the

kinetic energy during the initial phase of a collapsing cloud, when the core still has a lot of diffuse and relatively low-dense material (Traficante et al. 2018). The observed effective virial parameter $\alpha_{\rm eff}$ is less than $\alpha_{\rm vir}$ and we should be cautious in using the parameter α to represent the virial state of an observed core. However, the dense cores G01, G02 and G07 with 70-μm detection have $\alpha \sim 1$, which might be because of an enhancement of the velocity dispersion in more evolved cores, or because of stellar feedback. Our results suggest that a gas core is strongly unstable during the initial phase of collapse, and when a protostellar object is clearly visible, the core tends to stabilize.

3.3 YSO identification based on *WISE* near- and mid-infrared data

The near- and mid-infrared emission in the molecular cloud is originated from warm dust heated by embedded protostars. Therefore, we could use the infrared emission to characterize star formation activities. The high-sensitivity mid-infrared images (Fig. 4) from the *WISE* (Wright et al. 2010), including 3.4-, 4.6-, 12- and 22-μm wavelengths, allow us to trace the infrared emission from YSOs. Note that the *WISE* emission also has contributions from other types of infrared sources besides YSOs, such as foreground stars and extragalactic objects, which can be seen in projection towards the observed clouds.

To investigate the nature of the identified *WISE* sources, we employed the *WISE* colour criteria listed in Koenig & Leisawitz (2014). By using the uncertainty/signal-to-noise/chi-square criteria in Koenig & Leisawitz (2014), we selected the reliable point-source photometry in the ALLWISE catalogue within the G181 structures. The resultant catalogue, including *WISE* and 2MASS near- and mid-infrared colours and magnitudes, was used to identify YSOs. We also removed objects matching the criteria as likely star-forming galaxies, broad-line AGNs, AGB stars and CBe stars.
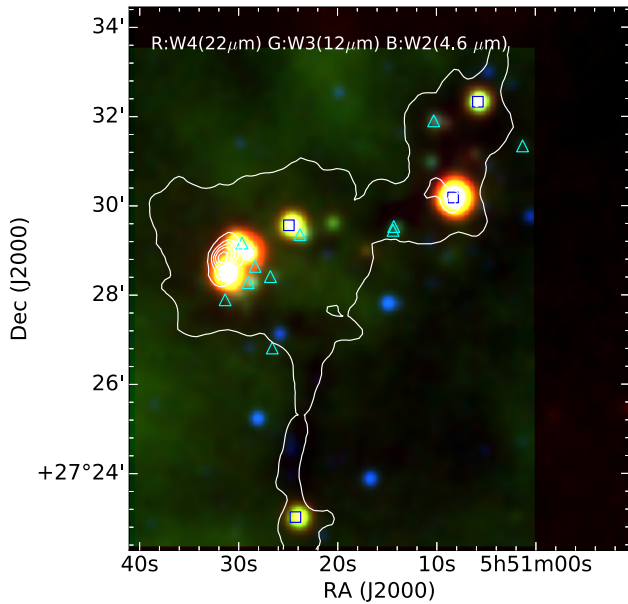
Figure 4. The three-colour map composed through W4 (22 µm), W3 (12 µm) and W2 (4.6 µm), shown as red, green and blue colours, respectively. The white contours display emission from the 250-µm map, ranging from 10 to 90 per cent, stepped by 15 per cent of the peak value (1080 MJy sr^{-1}). The blue squares are for Class I YSOs and cyan triangles are for Class II YSOs.
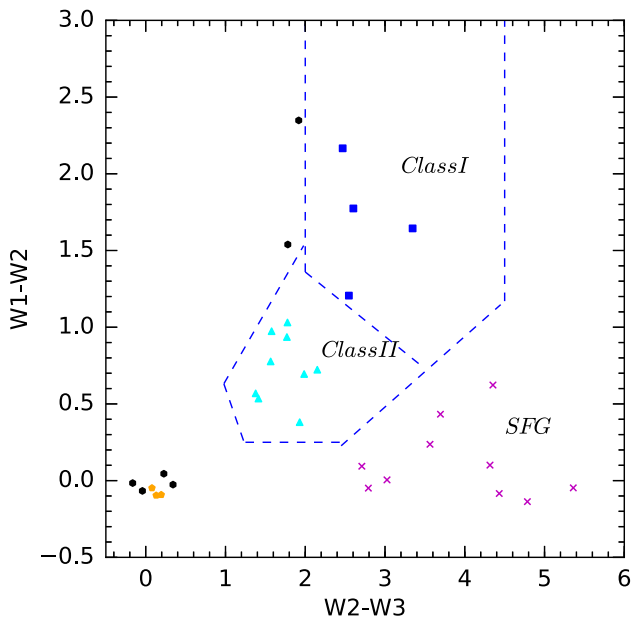
Figure 5. *WISE* colour–colour diagrams. YSOs located in regions enclosed by blue dashed lines are classified as Class I (blue squares) and Class II (cyan triangles), based on the criteria of Koenig & Leisawitz (2014). The black circles, orange hexagons and magenta crosses represent field stars, AGBs and star-forming galaxies (SFG), respectively.

As shown in Fig. 5, Class I YSOs (protostellar candidates) are the reddest objects, and are classified as such if their colours match the following criteria (Koenig & Leisawitz 2014):

W2 − W3 > 2.0;

W1 − W2 > −0.42 × (W2 − W3) + 2.2;
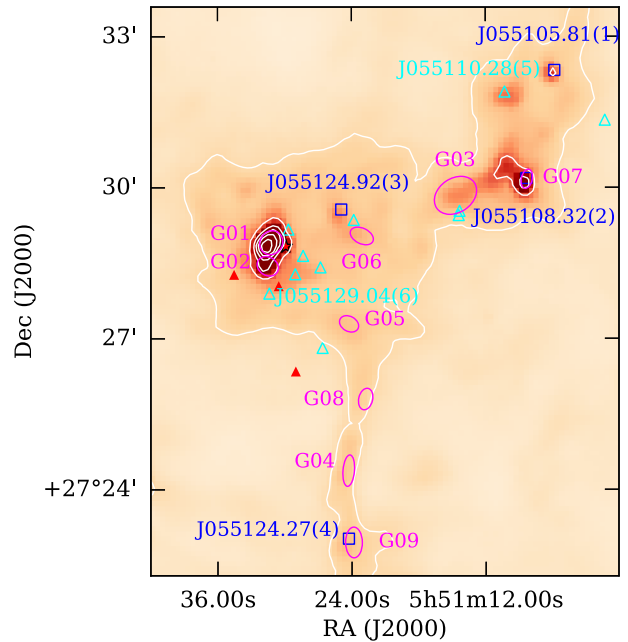
Figure 6. The background is the 250 µm continuum emission map. White contours display intensities of 250 µm continuum, ranging from 10 per cent to 90 per cent stepped by the 15 per cent of the peak value (1080 MJy sr^{-1}). Blue squares, cyan triangles and magenta ellipses respectively stand for Class I YSOs, Class II YSOs and SCUBA-2 compact sources. Three red triangles represent the Class II YSOs only identified using the method in Dewangan et al. (2017). The six labelled YSOs are fitted by the R17 model (see Section 3.4 for details).

W1 − W2 > 0.46 × (W2 − W3) − 0.9;

W2 − W3 < 4.5.

Class II YSOs (candidates of T Tauri stars and Herbig AeBe stars) are classified from the remaining pool of objects, if their colours match all the following criteria (Koenig & Leisawitz 2014):

W1 − W2 > 0.25;

W1 − W2 < 0.9 × (W2 − W3) − 0.25;

W1 − W2 > −1.5 × (W2 − W3) + 2.1;

W1 − W2 > 0.46 × (W2 − W3) − 0.9;

W2 − W3 < 4.5.

In addition, two more Class II YSOs candidates, with no photometric data in *WISE* band 3, are identified using the photometric data in *WISE* bands 1 and 2 and 2MASS data in the *H* and K_s bands, based on the additional criteria listed in Koenig & Leisawitz (2014). In this way, we have identified 15 (4 Class I and 11 Class II) YSOs in PGCC G181. As shown in Fig. 6, all the YSOs are distributed along the filamentary structures. Five Class II YSOs are located in the Fa substructure, and four Class I YSOs lie along the substructures Fb and Fc.

Previously, Dewangan et al. (2017) have identified 13 Class II and two Class I YSOs in the G181 region using the colour–colour criteria based on the 2MASS and GLIMPSE360 point-source data (Whitney et al. 2011). For comparison, we plot their classification diagram and the distribution of their YSOs in Fig. A2. We find that our method based on the *WISE* colours can classify most of these YSOs consistently, except for three Class II YSOs; this might be due to the lower resolution and sensitivity of the *WISE* data compared with the GLIMPSE360 photometric data. However, three new YSOs, J055105.81(Class I), J055108.32(Class I) and J055123.81, are found with our *WISE* colour criteria. This could

be because these YSOs, especially the Class I objects, are deeply embedded in dusty envelopes, and hence our classification criteria using the *WISE* data (with a longer wavelength) have a better chance of discovering them. If the three extra Class II YSOs identified by Dewangan et al. (2017) are included, we obtain a sample of 18 YSOs in G181. As presented in Fig. 6, we find that Class I YSOs J055108.32 and J055124.27 are associated with the dense cores G07 and G09, which further confirms that these two cores are in the evolution stage of forming protostars.

3.4 The parameters for YSOs

3.4.1 Models

Robitaille (2017, hereafter R17) presented an improved set of SED models for YSOs. In the R17 models, the coverage of parameter space is more uniform and wider than the model of Robitaille et al. (2006), and highly model-dependent parameters have been excluded. Moreover, the improved models are more suited to modelling far-infrared and submm flux intensities of the forming stars. The models are split into 18 different sets with increasing complexity. The model sets span a wide range of evolutionary stages, from the youngest deeply embedded protostars to pre-main-sequence stars with little or no discs.

3.4.2 Input data and SED fits

We constructed photometric SEDs for the identified YSOs using wavelengths ranging from 1.25 to 160 μm. Searching within 3 arcsec of the YSO positions in G181, we retrieved the *J*-, *H*- and K_s-band fluxes from the 2MASS All-Sky Point Source Catalogue (Skrutskie et al. 2006), the fluxes of IRAC bands 1 and 2 (3.6 and 4.5 μm) in the *Spitzer* GLIMPSE360 catalogue, and the mid-infrared bolometric fluxes from *WISE* (W3 and W4 bands) in the ALLWISE Source catalogue and PACS Point Source Catalogue in *Herschel*. In order to yield reliable results, the SED model fitting requires data at $\lambda > 12$ μm. For this reason, we carried out SED fitting only for sources that have data available in the *Herschel* PACS Point Source Catalogue. Such a subsample contains six sources out of the 18 identified YSOs in G181. The selected sources have been noted by source names in Fig. 6, which are distributed around the entire structure.

The distance was fixed to be 1.76 ± 0.04 kpc, and the A_v range was from 0 to 40 mag. The extinction law was the same as that used in Forbrich et al. (2010). The errors of the photometry data were adopted from the original source catalogue. We select all SED fittings that satisfy $\chi^2 - \chi^2_{best} < 3n_{data}$ as the reasonable results, where χ^2_{best} is the χ^2 of the best model for each model set and n_{data} is the number of data points. For each source, the resultant model set corresponds to the fitted SED having the lowest χ^2_{best} value. Fig. 7 shows the resultant model sets for the six fitted YSOs in G181.

3.4.3 Fit parameters

Table A1 lists the fitted parameters for YSOs using the best-fitting SED model sets. We estimated the mean values of A_v, T_{eff} and stellar radius $R_\star$ from all the fits satisfying the χ^2 cut in the chosen model sets. Then, we used the Stefan–Boltzmann law, assuming a solar T_{eff} of 5772 K, to estimate the stellar luminosity $L_\star$ using the model fitted values of T_{eff} and $R_\star$. Based on both the stellar $L_\star$ and T_{eff}, we further estimated the stellar mass for each YSO using the

pre-main-sequence tracks, which are for stars with metallicity of $Z = 0.02$ and mass range from 1.0 to 60 M$_\odot$ (Bernasconi 1996).

We roughly derived the mass for the YSOs by the least separation of each source away from the stellar track of the corresponding mass in the $\log_{10}(L_\star)$–$\log_{10}(T_{eff})$ space. Fig. 8 shows the stellar tracks and locations of six YSOs in the $\log_{10}(L_\star)$ versus $\log_{10}(T_{eff})$ diagram. The masses of the six YSOs are in the range of 1–5 M$_\odot$. Combined with Fig. 6, we find that the young YSOs (Class I) are mainly located in the substructures Fb and Fc, and most of the evolved YSOs (Class II) are around the Fa substructure. Furthermore, J055105.81+273219.0(1), J055108.32+273011.1(2) and J055110.28+273154.2(5) in the Fb substructure and J055124.27+272301.5(4) in the Fc substructure are located in evolutionary stages in the pre-main-sequence tracks earlier than the YSOs J055124.92+272933.9(3) and J055129.04+272816.8(6) around the Fa substructure. This is good evidence for sequential star formation in the filamentary structure of G181.

3.5 Dynamical structures

3.5.1 The integrated intensity of HCO^+ and N_2H^+ spectral lines

The low-*J* HCO$^+$ lines are sensitive to the gas with densities of the order of 10^5–10^6 cm^{-3}, which could be excellent tracers of the velocity field of molecular clouds (Qi et al. 2003). In addition, the N$_2$H$^+$(1–0) line, which has a critical density of $n_{crit} = 1.4 \times 10^5$ cm^{-3} at 10 K, can trace the cold dense cores well (Caselli et al. 2002). However, taking the radiative trapping into account, the effective critical density of N$_2$H$^+$(1–0) is pushed down to n_{crit} $\sim 1.0 \times 10^4$ cm^{-3} at 10 K (Shirley 2015). The FWHM beam size of the NRO 45-m telescope is about 18 arcsec at 90 GHz. Such a resolution is high enough to resolve the filaments with a typical width of 0.1 pc (Arzoumanian et al. 2011) at a distance of ~1.76 kpc.

From Fig. 9, we can see the distributions of the HCO$^+$(1–0) and N$_2$H$^+$(1–0) integrated intensities look similar to that of the dust. Dense cores and YSOs are mainly located on the region with higher column density and stronger HCO$^+$ (1–0) and N$_2$H$^+$ (1–0) emission. We find that the HCO$^+$(1–0) line reveals more extended structures, while the N$_2$H$^+$(1–0) line highlights the dense cores.

3.5.2 Channel maps of $HCO^+(1–0)$ molecular lines

In Fig. 10, we present the channel maps of the HCO$^+$(1–0) emission. The channel increment is 0.2 km s^{-1} in the range 0.6–3.9 km s^{-1}. The HCO$^+$(1–0) emission reveals a relative extended structure, in particular for the velocity range 1.7–2.4 km s^{-1}, which harbours the crowded YSOs and cores G01, G02 and G06. In the blueshifted velocity range 0.6−1.5 km s^{-1}, the emission mainly distributed along the southern subfilament Fc. The dense cores G04, G05 and G08 are associated with this component. As velocity increases from 2.4 to 3.9 km s^{-1}, the locations of strong emission regions have an overall trend of moving from the Fa substructure to the Fb substructure. The Fb substructure is mainly in the red end of the velocity range and contains G03 and five YSOs. The Fa substructure shows HCO$^+$(1–0) emission spanning from 1.5 to 3.9 km s^{-1}. It is obvious that the molecular gas is distributed velocity-coherently from the south-east to the north-west.

3.5.3 The centroid velocity and velocity width of the HCO^+ line

Fig. 11 shows the distribution of the line-of-sight centroid velocity and the FWHM linewidth of the HCO$^+$(1–0) line. We limited our
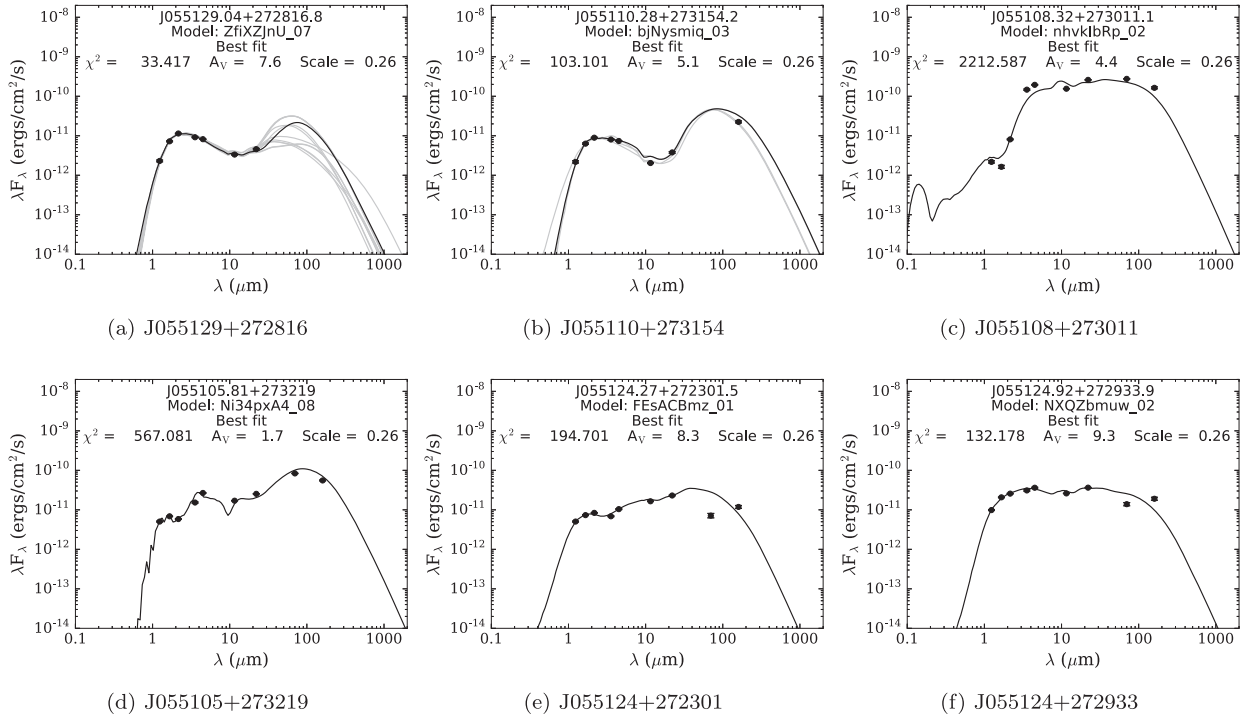
Figure 7. SED fits for six YSOs in G181.84 with available photometric data up to 160 μm, performed by the SED fitting tool using different YSO SED models in R17. The best fit is shown by the solid black line, and grey lines show all other fits that satisfy the criteria: $\chi^2 - \chi^2_{\text{best}} < 3n_{\text{data}}$.
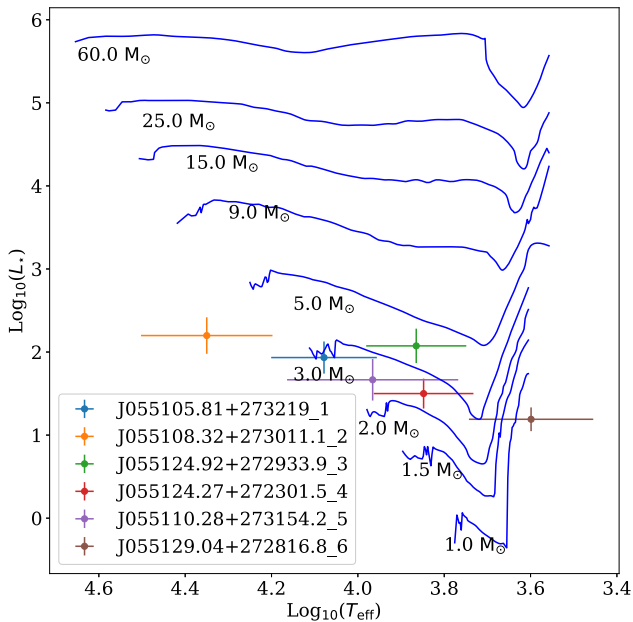
Figure 8. The $\log_{10}(L_\star)$ versus $\log_{10}(T_{\text{eff}})$ diagram displays the locations of YSOs (cross symbols) and the pre-main-sequence stellar tracks from Bernasconi & Maeder (1996) for different masses in blue. The errors in T_{eff} and $L_\star$ are also shown.

view to regions with T_{mb} larger than $\sim6\sigma$ (1.2 K). The value range of the V_{LSR} map is between 0.5 and 3.6 km s^{-1}. It is clear that the dense gas velocity in the Fb substructure is mainly redshifted, and varies smoothly along the subfilaments, while the Fc substructure becomes blueshifted. In the right panel, the FWHM velocity width

distributes between 0.5 and 2.2 km s^{-1}. We also found a notable increasing velocity width (FWHM) towards the Fa substructure, peaking at $\sim$2.15 km s^{-1}. The mean velocity widths for Fa, Fb and Fc are 0.98 ± 0.4, 0.69 ± 0.2 and 0.38 ± 0.17 km s^{-1}, respectively. This indicates that there are increasing star formation activities in the Fc, Fb and Fa substructures, which inject more energy to perturb the neighbouring gas.

The non-thermal velocity dispersion is derived from the observed linewidth using (Myers & Benson 1983)

$$(\sigma_{\text{NT}})^2 = (\sigma_{\text{obs}})^2 - (\sigma_{\text{T}})^2 \tag{5}$$

and

$$\sigma_{\text{NT}} = \sqrt{\frac{\Delta v_{\text{obs}}^2}{8\ln(2)} - \frac{k_B T_{\text{kin}}}{m_{\text{obs}}}}. \tag{6}$$

Here, σ_{NT}, σ_{obs} and σ_{T} are the non-thermal, observed and thermal velocity dispersion, respectively, Δv_{obs} represents the observed linewidth (the FWHM velocity width of HCO$^+$ fitted by the Gaussian model), k_B is the Boltzmann constant, T_{kin} is the kinetic temperature of the gas and m_{obs} means the mass of the observed molecule (29 a.m.u. for HCO$^+$). According to the dust temperature map in Fig. 2, we assume a gas kinematic temperature of 13 ± 2 K for Fa and 10 ± 1 K for Fb and Fc. The thermal dispersion of the gas corresponds to 0.04 $\pm$ 0.003 km s^{-1} (Fa) and 0.035 $\pm$ 0.002 (Fb and Fc). The derived non-thermal velocity dispersion is $\sim$0.414 km s^{-1} (Fa), 0.29 km s^{-1} (Fb) and 0.157 km s^{-1} (Fc). The corresponding mean $\sigma_{\text{NT}}/\sigma_{\text{T}}$ value is 10 ± 0.3 (Fa), 8.3 ± 0.5 (Fb) and 4.5 ± 0.3 (Fc). The Mach number, defined as the ratio between the non-thermal velocity dispersion and the sound speed, is about 1.9 for Fa, 1.5 for Fb and 0.8 for Fc. This indicates that the substructures Fa and Fb are mildly supersonic, while Fc is subsonic. Konstandin et al. (2016) studied the turbulent flows with Mach numbers ranging
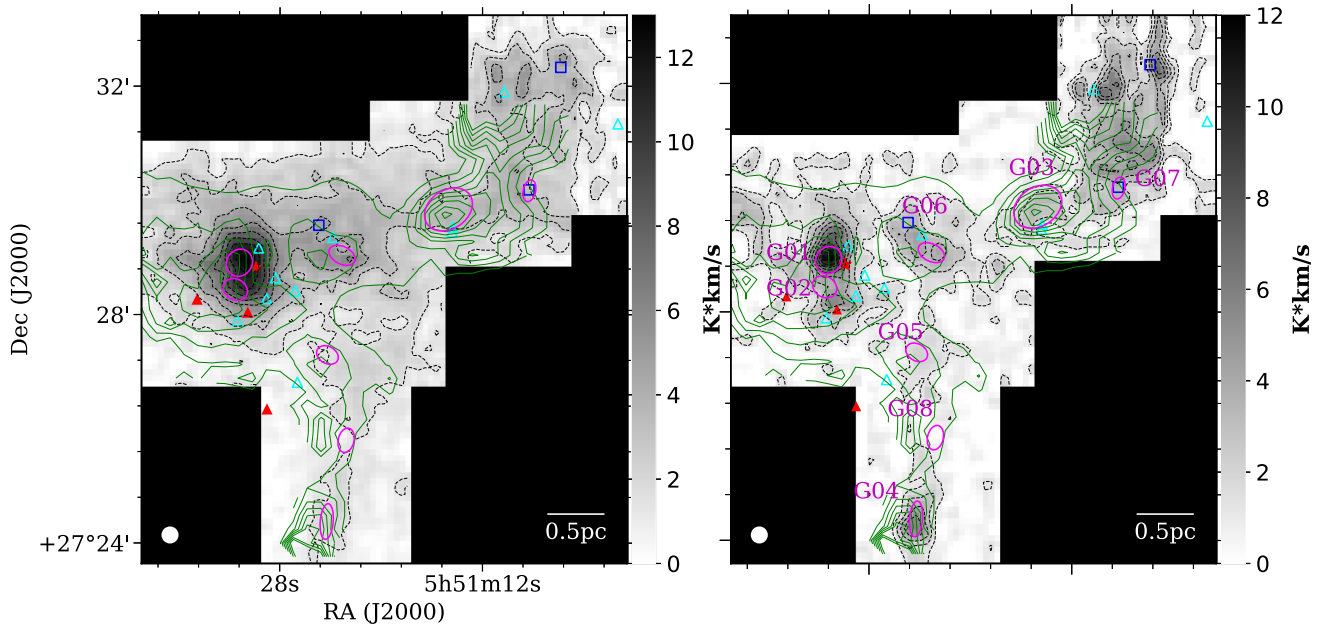
Figure 9. The grey-scale image represents the distribution of the integrated intensity between the velocity range (-15 8) km s^{-1} for the HCO$^+$(1–0) line (left panel) and the N$_2$H$^+$(1–0) line (right panel). Black contours range from 10 to 90 per cent, stepped by 10 per cent of the peak integrated intensity: 13 K km s^{-1} for HCO$^+$(1–0) and 12 K km s^{-1} for N$_2$H$^+$(1–0). The green contours denote the H$_2$ column density map obtained from the SED fitting based on the greybody radiation mode, ranging from 10 to 90 per cent, stepped by 10 per cent of the peak value (4 × 10^{22} cm^{-2}). The red star represents the source IRAS 05483+2728. The blue squares, cyan and red (*Spitzer*) triangles and magenta ellipses represent Class I YSOs, Class II YSOs and SCUBA-2 compact sources, respectively. The white circle in the left corner shows the beam size for the NRO 45-m telescope at 90 GHz.

from subsonic ($M \approx 0.5$) to highly supersonic ($M \approx 16$). They confirmed the relation between the density variance and the Mach number in molecular clouds. Such a relation implies that molecular clouds with higher Mach numbers present more extreme density fluctuations (Konstandin et al. 2016). This is consistent with the density enhancements in the Fa, Fb and Fc substructures. However, the large Mach numbers, especially in the Fa substructures, might also be due to feedback from star formation activities.

It should be noted that the HCO$^+$ line is usually not optically thin and, consequently, its linewidths can be broadened due to opacity (Sanhueza et al. 2012). In addition, the HCO$^+$ line has usually been used to evaluate the infall properties of a given star-forming region with blue-skewed line profiles (Sanhueza et al. 2012; Rygl et al. 2013; Yoo et al. 2018). As mentioned in Section 3.2.3, N$_2$H$^+$ is thought to be a better high-density tracer, and less affected by star formation activities. We have derived the velocity dispersion and centroid velocity of the N$_2$H$^+$ and HCO$^+$ lines for our sample of dense cores, as presented in Figs A3 and A4. The method used to fit the hyperfine structure of N$_2$H$^+$ has taken the opacity effects into account. We reveal that there is a decreasing trend of velocity dispersion traced by N$_2$H$^+$ from dense cores G01 and G02 in substructure Fa, G03 and G07 in substructure Fb, to G04 and G06 in substructure Fc. This further confirms the validation of the velocity dispersion gradient from the HCO$^+$ line. Because of the low S/N of N$_2$H$^+$ emission in dense core G05, its fitted velocity dispersion was not taken into account.

In addition, we found that the centroid velocities in dense cores derived from the N$_2$H$^+$(1–0) line are generally consistent with those derived from the HCO$^+$(1–0) line, except for G01, G02 and G03 with velocity offsets of 0.2–0.6 km s^{-1}. This might be due to the fact that HCO$^+$ traces motions of less dense gas compared with N$_2$H$^+$, because N$_2$H$^+$ tends to be more centrally distributed. We also compared the spectra of the HCO$^+$(1–0) line with the H^{13}CO$^+$(1–0)

lines for cores G01, G02 and G03. The centroid velocity traced by the two lines are consistent in G01, while the H^{13}CO$^+$ $J = 1-0$ profile in G02 shows double peaks and the centroid velocity of N$_2$H$^+$ matches that of the blueshifted peak. Because the critical densities of N$_2$H$^+$ and H^{13}CO$^+$ are similar, as listed in table 1 of Shirley (2015), the difference between the N$_2$H$^+$ and H^{13}CO$^+$ peak velocities in the G01, G02 and G03 cores might reflect the different spatial distributions of these two molecules.

4 DISCUSSION

4.1 Hierarchical network of filaments in 350-μm continuum emission

We used the FilFinder[10] algorithm based on the techniques of mathematical morphology (Koch & Rosolowsky 2015) to detect filamentary structures in the 350-μm map. Compared with other algorithms, FilFinder can not only identify the bright filaments, but also reliably extract a population of fainter striations (Koch & Rosolowsky 2015). The main process of the FilFinder algorithm includes the following steps: (i) the image is fitted with a lognormal distribution and flattened using an arctangent transform; (ii) the flattened data are smoothed using a Gaussian filter (0.05 pc for FWHM, half of the typical width of a filament; Arzoumanian et al. 2011); (iii) a mask of the filamentary structure is created in the smoothed image using an adaptive threshold; (iv) the filamentary structures are detected in the local brightness thresholds within the mask. The parameters of the thresholds are listed in the Appendix. In Fig. 12, we plot the skeletons of the subfilaments, colour-coded with the centroid velocities of the HCO$^+$(1–0) line. We find that

[10]https://github.com/e-koch/FilFinder
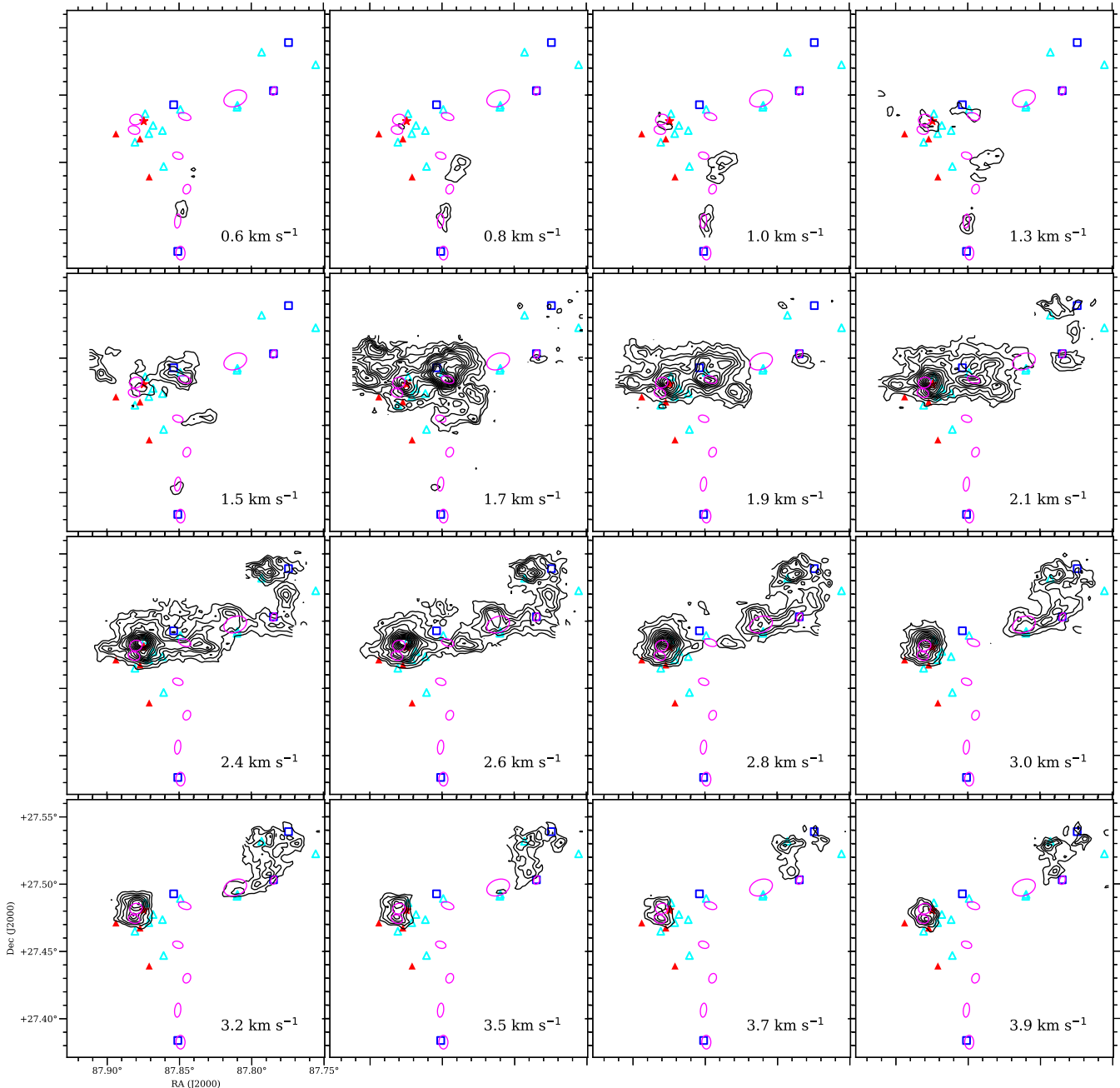
Figure 10. Channel maps of the HCO$^+$(1–0) line, with the contour levels from the 3σ ($\sim$0.2 K km s^{-1}) to the peak value in the interval of 1σ. The blue squares represent Class I YSOs, cyan and red (*Spitzer*) triangles stand for the Class II YSOs and magenta ellipses for the SCUBA-2 compact sources.

the skeletons of subfilaments for the Fb and Fc substructures merge at the Fa substructure. In addition, combining the left panel in Fig. 11 with Fig. 12, it is clear that the southern substructure (Fc) is blueshifted (0.5–2.5 km s^{-1}), and the northern substructure (Fb) is redshifted (2.5–3.5 km s^{-1}). The Fb and Fc substructures present clear velocity gradients. The SCUBA-2 dense cores are mainly distributed along the skeletons.

4.2 The velocity gradients along subfilaments

In Fig. 13, we present the centroid-velocity profiles of the sub-filamentary skeletons Fb and Fc. The merging point of Fb and Fc skeletons in the Fa substructure is defined as the zero-point on the *x*-

axis. The *x*-axis value (Fig. 13) of a pixel on the skeleton represents its distance from the zero-point integrated along the spine lines (Fig. 12). It is evident that the subfilaments Fb and Fc exhibit both global and local velocity gradients. For the Fb subfilament, the global velocity gradients are about 0.8 $\pm$ 0.05 km s^{-1} pc^{-1} from 0.5 to 2.5 pc of the *x*-axis value, and the local velocity gradients near the Fa substructure are up to 1.2 $\pm$ 0.1 km s^{-1} pc^{-1} from 0.0 to 0.5 pc in skeleton length. The Fc subfilament shows velocity gradients of $\sim$1.0 $\pm$ 0.05 km s^{-1} within a range of 0.0–1.7 pc on the *x*-axis, and 1.3 $\pm$ 0.1 km s^{-1} pc^{-1} in the range of 0.0–0.6 pc. It is evident that the local velocity gradients around substructure Fa, including G01, G02 and seven YSOs, are larger than the global velocity gradients along the subfilaments Fb and Fc. In addition,
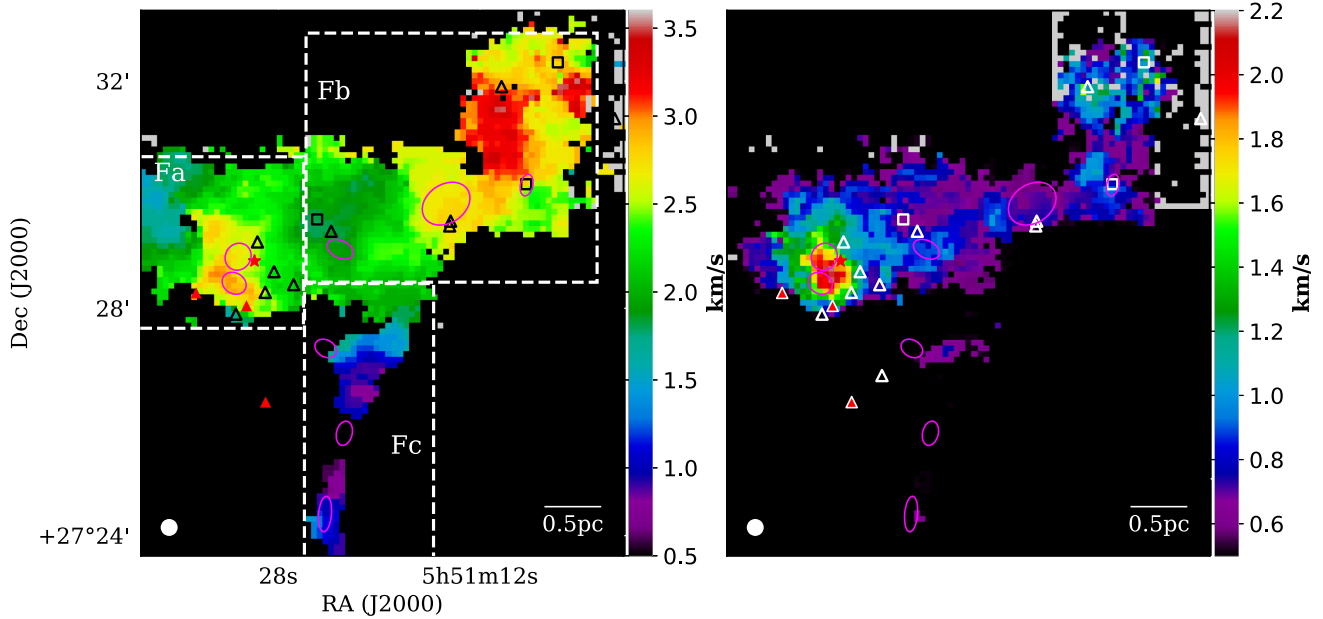
Figure 11. Left: the velocity field of G181 structures. Right: the velocity width distribution map for G181. Both are obtained from Gaussian fitting of the HCO^+(1–0) line. The squares represent Class I YSOs, triangles stand for the Class II YSOs and magenta ellipses for the SCUBA-2 compact sources. The white circle in the bottom-left corner shows the beam size for the NRO 45-m telescope at 90 GHz.
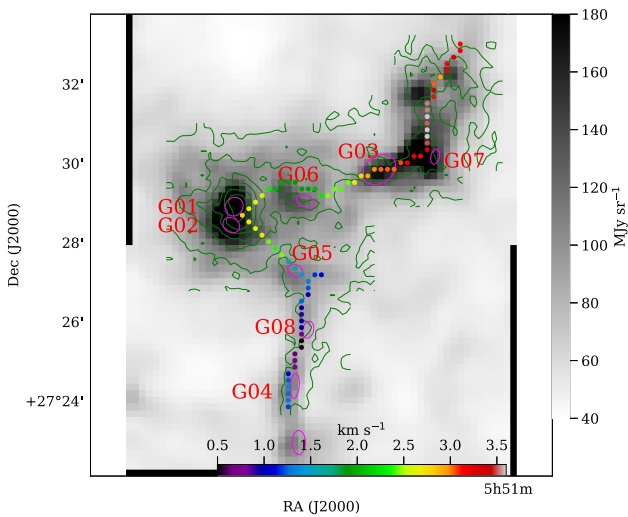
Figure 12. The skeletons of the filament network extracted with the Fil-Finder algorithm, colour-coded with the centroid velocities of the HCO^+(1–0) spectral line. Magenta ellipses represent the SCUBA-2 compact sources. Green contours show the distribution of the HCO^+ integrated intensity, levels are from 10 to 90 per cent with the interval of 15 per cent of the peak value (13 K km s^{-1}).

we also find that the dense cores G01 and G02 appear to locate near the maxima of velocity profiles along the subfilaments, while there is almost a quarter phase shift between the densities (i.e. dense cores G03, G05, G04, G06 and G08) and velocities. This suggests that the continuum peaks have an influence on the dynamics of the surrounding gas (Hacar & Tafalla 2011; Liu et al. 2016b; Yuan et al. 2018).

As shown in Fig. 1, G181 is located on the northern end of the EFS S242. For the longer filaments with the aspect ratio, $A_o \gtrsim 5.0$, global collapse would be end-dominated; the materials are
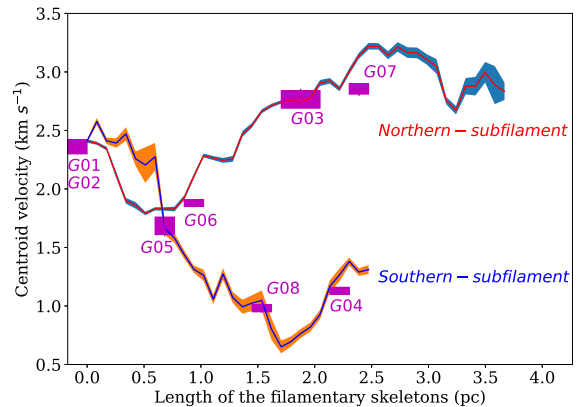
Figure 13. The centroid velocity of HCO^+(1–0) emission distributed along the skeletons of the filament network extracted by FilFinder. The zero-point on the *x*-axis is the merging point for the northern substructure (Fb) and southern substructure (Fc). The *x*-axis increasing direction is from the merging point at the Fa substructure along the subskeletons to the northern and southern end. The shaded area along the lines represents the error limits for the fitted centroid velocity. The magenta boxes show the dense cores, and the widths of the boxes represent the spatial distribution of dense cores along the filaments. The box heights represent the range of average centroid velocity for dense cores fitted by the HCO^+(1–0) and N_2H^+(1–0) lines, as shown in Figs A3 and A4.

preferentially accelerated into the both ends. The end-clumps were given more momentum, and further approach the centre of filaments in an asymptotic inward speed, sweeping up gas mass as they approach (Pon et al. 2011, 2012). Moreover, Clarke & Whitworth (2015) investigated the end-dominated collapse in filaments, and suggested that due to gravitational attraction of the end-clumps, the gas ahead of end-clumps was immediately accelerated towards end-clumps. Dewangan et al. (2017) concluded that the observed results of massive clumps and the clusters of YSOs toward both ends of

EFS S242 were consistent with the prediction of the end-dominated collapse model. The global velocity gradients along Fb and Fc in the northern end of EFS S242 might be caused by the gas motion in the end-dominated collapse.

4.3 Gravitational fragmentation of subfilaments

As shown in Fig. 12, G181 contains subfilaments with nine dense cores embedding in them. To investigate the fragmentation of subfilaments and hence the formation of dense cores, we compare the substructures of G181 with the model of a collapsing isothermal cylinder, supported by either thermal or non-thermal motions. André et al. (2013) has suggested that thermally supercritical filaments, where the mass per unit length is greater than the critical value ($M_{line, crit}$; i.e. $M_{line} > M_{line, crit}$), are associated with pre-stellar clumps/cores and star formation activities. However, there are few *Herschel* pre-stellar clumps/cores and embedded protostars associated with thermally subcritical filaments ($M_{line} < M_{line, crit}$).

For thermal support, the critical mass per unit length ($M_{line, crit} = 2c_s^2/G$, where c_s is the isothermal sound speed and G is the gravitational constant) is needed for a filament to be gravitationally unstable to radial contraction and fragmentation along its length (Inutsuka & Miyama 1997). The thermal critical line mass $M_{line, crit}$ is $\sim$16 $M_\odot$ pc^{-1} $\times$ ($T_{gas}/10$ K) for gas filaments (André et al. 2014). The filamentary structures of G181 have an observed mass per unit length of $\sim$200 $M_\odot$ pc^{-1} (Dewangan et al. 2017). The observed value largely exceeds the critical value of $\sim$16–48 $M_\odot$ pc^{-1} (at T = 10–30 K).

Taking into account additional supports from turbulent pressure, the total one-dimensional velocity dispersion is calculated with the following equation (Fuller & Myers 1992)

$$\sigma_{TOT} = \sqrt{\frac{\Delta v_{obs}^2}{8 \ln(2)} + k_B T_{kin} \left(\frac{1}{\mu m_H} - \frac{1}{m_{obs}} \right)}, \tag{7}$$

where m_H is the mass of a hydrogen atom, and $\mu = 2.33$ is the atomic weight of the mean molecule. According to the observed linewidth and dust temperatures mentioned in Section 3.5.2, we calculated the one-dimensional velocity dispersions of σ_{TOT}, which are $\sim$0.47 $\pm$ 0.07, 0.35 $\pm$ 0.05 and 0.25 $\pm$ 0.07 km s^{-1}, respectively, for Fa, Fb and Fc. The uncertainties are estimated based on a $\sim$15 per cent error in the temperature and a $\sim$20 per cent error in the observed linewidth. We calculated the critical line mass supported by both thermal and non-thermal contributions using (Fiege & Pudritz 2000)

$$(M/L)_{crit} = \frac{2\sigma_{TOT}^2}{G} \tag{8}$$

The derived critical line masses supported by the thermal and non-thermal pressure are 101 $\pm$ 15, 56 $\pm$ 8 and 28 $\pm$ 4 $M_\odot$ pc^{-1}, for Fa, Fb and Fc, respectively. The observed masses per unit length ($\sim$200 $M_\odot$ pc^{-1}) are still a factor of 2–7 times larger than the critical values. Therefore, the dense cores in G181 might be formed through cylindrical fragmentation.

4.4 Sequential star formation

In Section 3, based on the evolutionary states of dense cores and YSOs, we find that dense cores and YSOs around the Fa substructure (two protostars and seven Class II YSOs) are at relatively later stages of evolution than those in the Fb (two pre-stellar candidates, three Class I YSOs and five Class II YSOs)

and Fc (three pre-stellar candidates, one Class I YSOs and two Class II YSOs) substructures, which provide evidence for sequential star formation in the structures of PGCC G181. We also found inhomogeneous distribution of the physical properties in the Fa, Fb and Fc substructures of G181, including the H$_2$ column density, dust temperature and velocity dispersion. Heitsch et al. (2008) studied numerically the formation of molecular clouds in large-scale colliding flows including self-gravity. Their model emphasized that large-scale filaments were mostly driven by global gravity, and local collapses were triggered by a combination of strong thermal and dynamical instabilities, which further caused cores to form.

Pon et al. (2011, 2012) pointed out that the global collapse time-scales of molecular clouds were decreasing outward in the edges. This leads to material preferentially accelerating on to the edges. Such a density enhancement occurs in the periphery of a cloud, and it can further trigger local collapse to form stars. In addition, the edge-driven collapse mode is mainly dominant in filaments with aspect ratios larger than 5. These filaments can also induce local collapse more easily by small perturbations (Pon et al. 2012). As pointed out by Dewangan et al. (2017), the EFS S242 might be a good example for the end-dominated collapse. We also find sequential star formation activities in the northern end of S242. The dense cores and YSOs in the Fb and Fc substructures are in younger evolutionary stages than those in the Fa substructure (two protostars and seven Class II YSOs), and the star formation activities in Fb, including two pre-stellar candidates, three Class I YSOs, and five Class II YSOs are more active than the Fc substructures (three pre-stellar candidates, one Class I YSOs, and two Class II YSOs). Therefore, we suggest that the star formation activities in the Fa, Fb and Fc substructures are progressively taking places in a sequence, following the order of the local density enhancements being built up gradually in the Fa, Fb and Fc substructures. Such a picture is consistent with the scenario of the end-dominated collapse model.

5 CONCLUSIONS

We have used the *Herschel* (70–500 μm), SCUBA-2 (850 μm) and *WISE* (3.4, 4.6, 12 and 22 μm) continuum maps and HCO$^+$(1–0) and N$_2$H$^+$(1–0) line data to study star formation in the filamentary structures of PGCC G181, which is sited at the northern end of the extended filamentary structure S242. The main results are as follows.

(i) We obtained an H$_2$ column density map (1.0, 4.0) $\times$ 10^{22} cm^{-2} and a dust temperature map (8, 16) K from SED fitting of *Herschel* (160–500 μm) and SCUBA-2 850-μm data, based on the greybody radiation model.

(ii) Nine compact sources have been identified from the SCUBA-2 850-μm map, including four protostellar and five pre-stellar candidates. Their physical parameters, including equivalent radius, dust temperature, column density, volume density, luminosity and mass are derived using SED fitting. The characteristics of the velocity dispersion, excitation temperature and optical depth are estimated by fitting the N$_2$H$^+$(1–0) spectral line. In addition, 18 YSOs, including four Class I YSOs and 14 Class II YSOs, are found in the G181 region based on the near- and mid-infrared colours obtained from the *WISE*, *Spitzer* and 2MASS catalogues.

(iii) We report observations of the HCO$^+$(1–0) and N$_2$H$^+$(1–0) spectral lines toward G181. We find that the distribution of the HCO$^+$(1–0) integrated intensities is consistent with to that of the dust emission, while the N$_2$H$^+$(1–0) emission is concentrated near

the dense cores. The dense cores and YSOs are mainly distributed along the filamentary structures of G181, and located in regions with higher column densities and stronger $HCO^+(1-0)$ and $N_2H^+(1-0)$ emission.

(iv) We find a notable increasing velocity dispersion towards the Fa substructure. The substructures Fa and Fb are mildly supersonic, while the Fc substructure is subsonic. In addition, we also detected velocity gradients of 0.8 ± 0.05 and 1.0 ± 0.05 km s^{-1} pc^{-1} for the Fb and Fc subfilaments, respectively, while the value for the Fa substructure is up to 1.2 km s^{-1} pc^{-1}. The global velocity gradients along the substructures Fb and Fc might be caused by the gas motion in the end-dominated collapse of filaments.

(v) We derive the critical mass per unit length for each subfilament in both thermal and non-thermal support cases. The values are 101 ± 15 M$_\odot$ pc^{-1} (Fa), 56 ± 8 M$_\odot$ pc^{-1} (Fb) and 28 ± 4 M$_\odot$ pc^{-1} (Fc). The observed masses per unit length ($\sim$200 M$_\odot$ pc^{-1}) are a factor of 2–7 times larger than the critical value of each subfilament, suggesting that the dense cores in G181 might be formed through cylindrical fragmentation.

(vi) We find evidence for sequential star formation in the filamentary structures of G181. The dense cores and YSOs located in the Fb and Fc substructures are younger than those in the Fa substructure. In addition, the star formation activities are gradually progressive in the Fa, Fb and Fc substructures, which are consistent with the materials being accelerated into the ends and then further inwards to the centre of the filament S242 in an end-dominated collapse.

ACKNOWLEDGEMENTS

REFERENCES

Ade P. A. R. et al., 2011, A&A, 536, A7

André P., 2017, Comptes Rendus Geoscience, 349, 187

André P., Könyves V., Arzoumanian D., Palmeirim P., Peretto N., 2013, in Kawabe R., Kuno N., Yamamoto S., eds, ASP Conf. Ser. Vol. 476, New Trends in Radio Astronomy in the ALMA Era: The 30th Anniversary of Nobeyama Radio Observatory, Astron. Soc. Pac., San Francisco, p. 95

André P., Di Francesco J., Ward-Thompson D., Inutsuka S-I., Pudritz R. E., Pineda J. E., 2014, in Beuther H., Klessen R. S., Dullemond C. P., Henning T., eds, Protostars and Planets VI. Univ. Arizona Press, Tuscon AZ, p. 27

Arzoumanian D. et al., 2011, A&A, 529, L6

Arzoumanian D. et al., 2019, A&A, 621, A42

Bergin E. A., Ciardi D. R., Lada C. J., Alves J., Lada E. A., 2001, ApJ, 557, 209

Bergin E. A., Alves J., Huard T., Lada C. J., 2002, ApJ, 570, L101

Bernasconi P. A., 1996, A&AS, 120, 57

Bernasconi P. A., Maeder A., 1996, A&A, 307, 829

Berry D. S., 2015, Astronomy and Computing, 10, 22

Berry D. S., Reinhold K., Jenness T., Economou F., 2007, in Shaw R. A., Hill F., Bell D. J., eds, ASP Conf. Ser. Vol. 376, Astronomical Data Analysis Software and Systems XVI, Astron. Soc. Pac., San Francisco, p. 425

Bintley D. et al., 2014, Proc. SPIE, 9153, 915303

Caselli P., Benson P. J., Myers P. C., Tafalla M., 2002, ApJ, 572, 238

Clarke S. D., Whitworth A. P., 2015, MNRAS, 449, 1819

Contreras Y. et al., 2013, A&A, 549, A45

Contreras Y. et al., 2018, ApJ, 861, 14

Contreras Y., Garay G., Rathborne J. M., Sanhueza P., 2016, MNRAS, 456, 2041

Daniel F., Dubernet M.-L., Meuwly M., Cernicharo J., Pagani L., 2005, MNRAS, 363, 1083

Dewangan L. K., Baug T., Ojha D. K., Janardhan P., Devaraj R., Luna A., 2017, ApJ, 845, 34

di Francesco J., Evans N. J., II, Caselli P., Myers P. C., Shirley Y., Aikawa Y., Tafalla M., 2007, in Reipurth B., Jewitt D., Keil K., eds, Protostars and Planets V. Univ. Arizona Press, Tuscon AZ, p. 17

Dunham M. M., Crapsi A., Evans N. J., II, Bourke T. L., Huard T. L., Myers P. C., Kauffmann J., 2008, ApJS, 179, 249

Eden D. J. et al., 2017, MNRAS, 469, 2163

Eden D. J. et al., 2019, MNRAS, 485, 2895

Fiege J. D., Pudritz R. E., 2000, MNRAS, 311, 85

Forbrich J., Tappe A., Robitaille T., Muench A. A., Teixeira P. S., Lada E. A., Stolte A., Lada C. J., 2010, ApJ, 716, 1453

Frerking M. A., Langer W. D., Wilson R. W., 1982, ApJ, 262, 590

Fuller G. A., Myers P. C., 1992, ApJ, 384, 523

Ginsburg A., Mirocha J., 2011, PySpecKit: Python Spectroscopic Toolkit, Astrophysics Source Code Library(ascl:1109.001)

Gutermuth R. A., Megeath S. T., Myers P. C., Allen L. E., Pipher J. L., Fazio G. G., 2009, ApJS, 184, 18

Hacar A., Tafalla M., 2011, A&A, 533, A34

Hacar A., Tafalla M., Forbrich J., Alves J., Meingast S., Grossschedl J., Teixeira P. S., 2018, A&A, 610, A77

Heitsch F., Hartmann L. W., Slyz A. D., Devriendt J. E. G., Burkert A., 2008, ApJ, 674, 316

Hildebrand R. H., 1983, QJRAS, 24, 267

Holland W. S. et al., 2013, MNRAS, 430, 2513

Hunter D. A., Massey P., 1990, AJ, 99, 846

Inutsuka S-i., Miyama S. M., 1997, ApJ, 480, 681

Johnstone D. et al., 2017, ApJ, 836, 132

Kainulainen J., Stutz A. M., Stanke T., Abreu-Vicente J., Beuther H., Henning T., Johnston K. G., Megeath S. T., 2017, A&A, 600, A141

Kauffmann J., Bertoldi F., Bourke T. L., Evans N. J., II, Lee C. W., 2008, A&A, 487, 993

Kauffmann J., Pillai T., Shetty R., Myers P. C., Goodman A. A., 2010, ApJ, 712, 1137

Kauffmann J., Pillai T., Goldsmith P. F., 2013, ApJ, 779, 185

Kim J. et al., 2017, ApJS, 231, 9

Koch E. W., Rosolowsky E. W., 2015, MNRAS, 452, 3435

Koenig X. P., Leisawitz D. T., 2014, ApJ, 791, 131

Konstandin L., Schmidt W., Girichidis P., Peters T., Shetty R., Klessen R. S., 2016, MNRAS, 460, 4483

Launhardt R. et al., 2013, A&A, 551, A98

Liu T. et al., 2016a, ApJS, 222, 7

Liu T. et al., 2016b, ApJ, 824, 31

Liu T. et al., 2018a, ApJS, 234, 28

Liu T. et al., 2018b, ApJ, 859, 151

Liu T., Wu Y., Zhang H., 2012, ApJS, 202, 4

Li P. S., Klein R. I., McKee C. F., 2016, in Jablonka P., André P., van der Tak F., eds, Proc. IAU Symp. 315, From Interstellar Clouds to Star-Forming Galaxies: Universal Processes?, Kluwer, Dordrecht, 103

MacLaren I., Richardson K. M., Wolfendale A. W., 1988, ApJ, 333, 821

Meng F., Wu Y., Liu T., 2013, ApJS, 209, 37

Molinari S. et al., 2010, A&A, 518, L100

Moore T. J. T. et al., 2015, MNRAS, 453, 4264

Myers P. C., Benson P. J., 1983, ApJ, 266, 309

Nordhaus M. K. et al., 2008, in Frebel A., Maund J. R., Shen J., Siegel M. H., eds, ASP Conf. Ser. Vol. 393, New Horizons in Astronomy. Astron. Soc. Pac., San Francisco, p. 243

Ohashi S., Sanhueza P., Sakai N., Kandori R., Choi M., Hirota T., Nguy#, 7877n-Lu'o'ng Q., Tatematsu K., 2018, ApJ, 856, 147

Ossenkopf V., Henning T., 1994, A&A, 291, 943

Pon A., Johnstone D., Heitsch F., 2011, ApJ, 740, 88

Pon A., Toalá J. A., Johnstone D., Vázquez-Semadeni E., Heitsch F., Gómez G. C., 2012, ApJ, 756, 145

Qi C., Kessler J. E., Koerner D. W., Sargent A. I., Blake G. A., 2003, ApJ, 597, 986

Qian L., Li D., Goldsmith P. F., 2012, ApJ, 760, 147

Reid M. J., Dame T. M., Menten K. M., Brunthaler A., 2016, ApJ, 823, 77

Rivera-Ingraham A. et al., 2016, A&A, 591, A90

Robitaille T. P., 2017, A&A, 600, A11 (R17)

Robitaille T. P., Whitney B. A., Indebetouw R., Wood K., Denzmore P., 2006, ApJS, 167, 256

Robitaille T. P. et al., 2013, A&A, 558, A33

Rygl K. L. J., Wyrowski F., Schuller F., Menten K. M., 2013, A&A, 549, A5

Sanhueza P., Jackson J. M., Foster J. B., Garay G., Silva A., Finn S. C., 2012, ApJ, 756, 60

Schneider N. et al., 2012, A&A, 540, L11

Schöier F. L., van der Tak F. F. S., van Dishoeck E. F., Black J. H., 2005, A&A, 432, 369

Schuller F. et al., 2009, A&A, 504, 415

Shirley Y. L., 2015, PASP, 127, 299

Skrutskie M. F. et al., 2006, AJ, 131, 1163

Traficante A., Fuller G. A., Billot N., Duarte-Cabral A., Merello M., Molinari S., Peretto N., Schisano E., 2017, MNRAS, 470, 3882

Traficante A., Lee Y-N., Hennebelle P., Molinari S., Kauffmann J., Pillai T., 2018, A&A, 619, L7

Wang K., Testi L., Ginsburg A., Walmsley C. M., Molinari S., Schisano E., 2015, MNRAS, 450, 4043

Wang K., Testi L., Burkert A., Walmsley C. M., Beuther H., Henning T., 2016, ApJS, 226, 9

Whitney B. et al., 2011, Amer. Astron. Soc. Meeting Abstracts, 217, 241.16

Williams J. P., 1994, Bull. Amer. Astron. Soc. , 26, 1477

Womack M., Ziurys L. M., Sage L. J., 1993, ApJ, 406, L29

Wright E. L. et al., 2010, AJ, 140, 1868

Wu Y., Liu T., Meng F., Li D., Qin S-L., Ju B.-G., 2012, ApJ, 756, 76

Yoo H., Kim K-T., Cho J., Choi M., Wu J., Evans N. J., II, Ziurys L. M., 2018, ApJS, 235, 31

Yuan J. et al., 2017, ApJS, 231, 11

Yuan J. et al., 2018, ApJ, 852, 12

Zhang C-P. et al., 2018, ApJS, 236, 49

## APPENDIX A: THE CRITICAL PARAMETERS OF THE THRESHOLDS IN FILFINDER

verbose = True,
   smooth_size = 0.05*u.pc,
   size_thresh = 2000*u.arcsec^2,
   glob_thresh = 50,
   fill_hole_size = 0.3*u.pc^2,
   border_masking = False
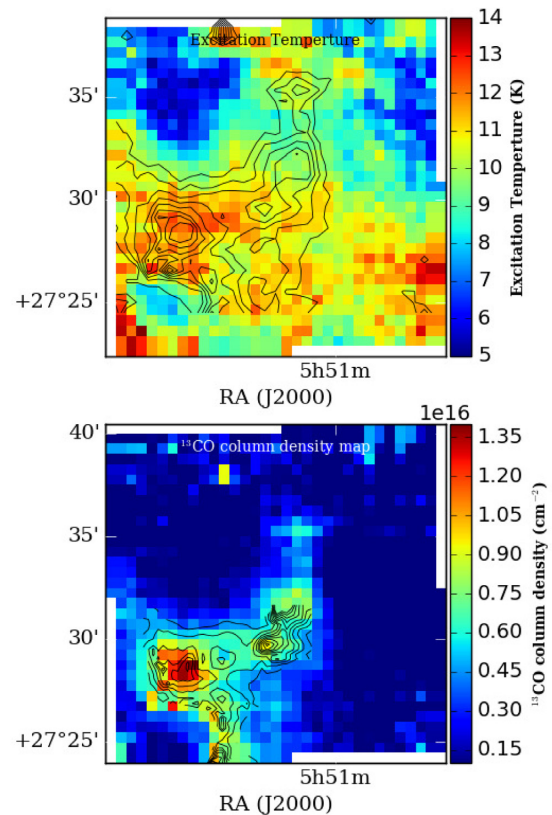
Figure A1. Upper panel: excitation temperature map, black contours represent the ^{13}CO column density, levels are from 20 to 90 per cent by the interval of 10 per cent of the peak value of 1.4×10^{16} cm^{-2}. Lower panel: ^{13}CO column density map. The overlaid black contours represent the H$_2$ column density derived by the SED fitting, levels are from 10 to 90 per cent by the interval of 10 per cent of the peak value (4.0×10^{22} cm^{-2}).
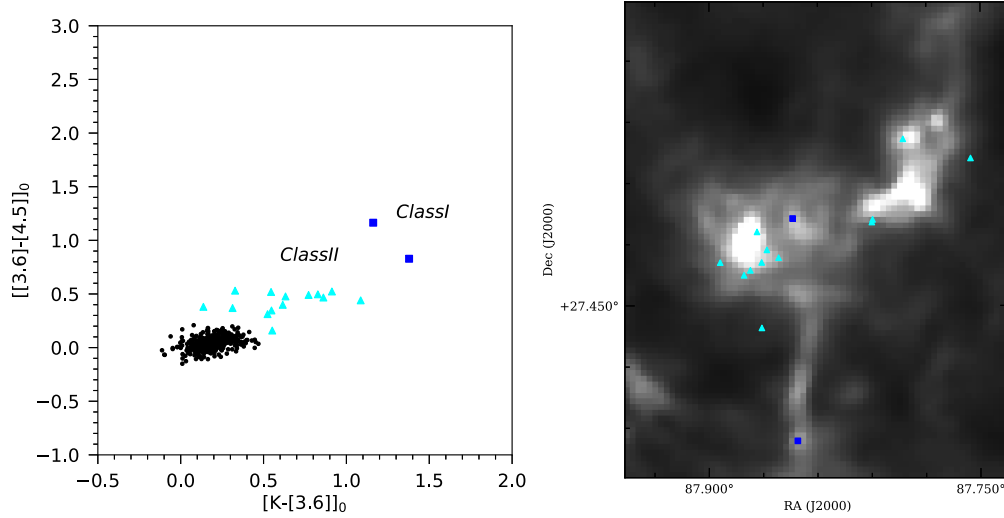
Figure A2. Left plane: the YSOs were identified by the 2MASS and GLIMPSE360 photometric data from 1 to 5 μm by the dereddened colour–colour space ($[K–[3.6]]_0$ and $[[3.6]–[4.5]]_0$). The detailed process was presented in Dewangan et al. (2017) and Gutermuth et al. (2009). Right plane: the distribution of the YSOs identified by the 2MASS and GLIMPSE360 photometric data in the 250-μm continuum map. The blue squares represent Class I YSOs and cyan triangles stand for Class II YSOs.
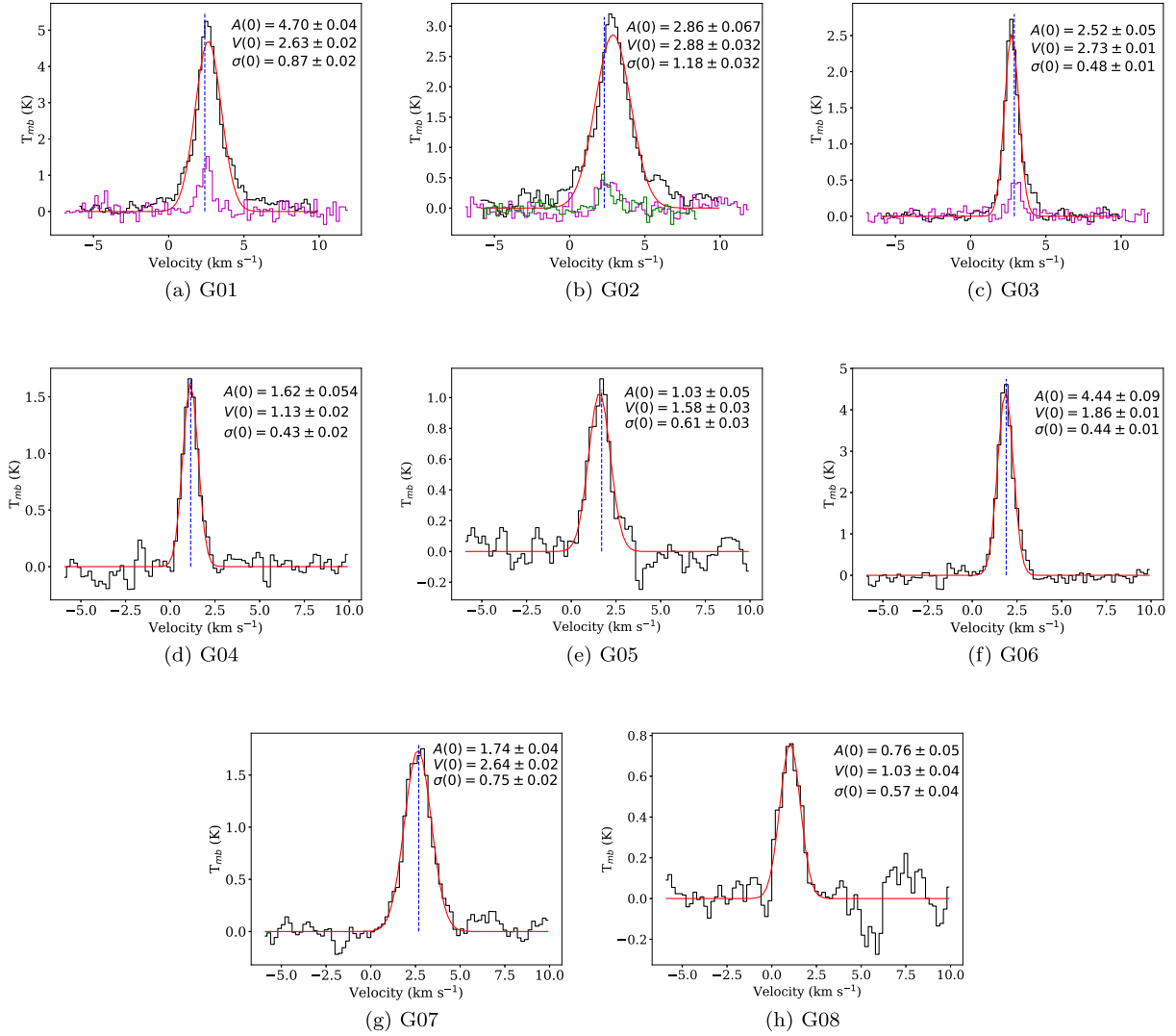
Figure A3. HCO$^+$(1–0) line profile for G01–G08 dense cores in G181. The blue vertical lines represent the corresponding velocity fitted by the hyperfine structure of the N$_2$H$^+$(1–0) line. The magenta profiles in G01–G03 are the H^{13}CO$^+$(1–0) line. The green profile in G02 is the highest-frequency component of the N$_2$H$^+$(1–0) line.
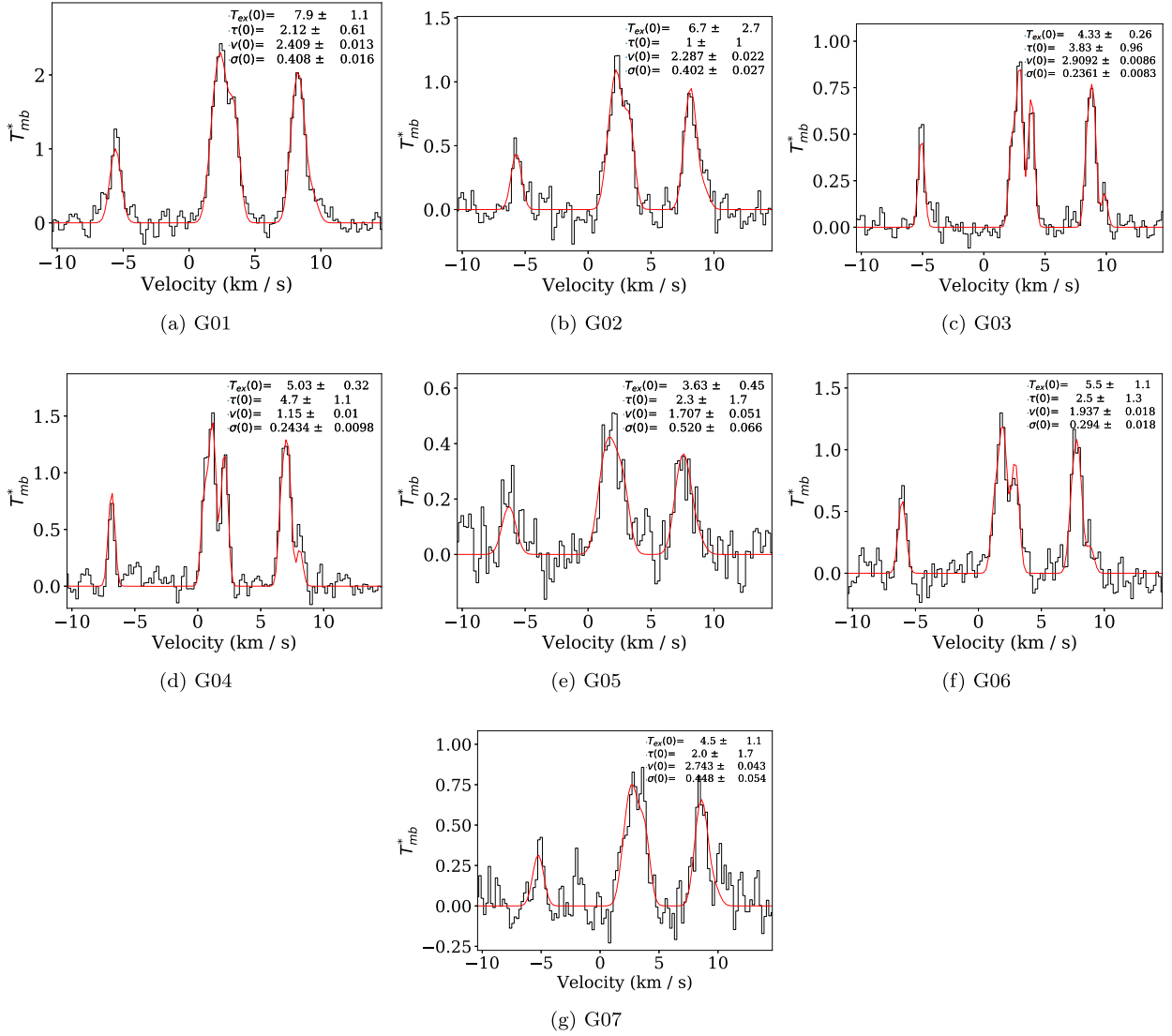
Figure A4. $N_2H^+(1-0)$ line profiles for G01–G07 dense cores in G181.

Table A1. The fitted parameters for YSOs using the best-fitting SED model set.

Source name	A_v / Envelope$_{rc}$	Scale / Cavity$_{power}$	$Star_r$ / Cavity$_{\theta_0}$	$Star_T$ / Cavity$_{\rho_0}$	Disk$_{mass}$ / Disk$_{rmin}$	Disk$_{rmax}$ / Envelope$_{rmin}$	Disk$_\beta$ / Ambient$_{density}$	Disk$_p$ / Ambient$_T$	Disk$_{h100}$ / Scattering	Envelope$_{\rho_0}$ / Inclination
J055105.81+273219.0	6.832	0.255	2.153e+00	1.198e+04	1.085e−02	1.044e+03	1.145e+00	−5.010e−02	3.416e+00	1.185e−22
	1.044e+03	1.961e+00	7.617e+00	1.782e−23	1.805e+00	1.805e+00	1.000e−23	1.000e+01	1.000e+00	1.145e+00
J055108.32+273011.1	5.607	0.255	8.348e−01	2.239e+04	3.554e−02	1.979e+03	1.151e+00	−9.120e−01	8.123e+00	7.537e+00
							1.000e−23	1.000e+01	1.000e+00	2.631e+01
J055124.92+272933.9	9.294	0.255	6.762e+00	7.325e+03	7.344e−04	5.733e+01	1.211e+00	−1.768e+00	4.691e+00	1.373e−23
	5.733e+01	1.249e+00	6.471e+00	1.409e−22	2.322e+00	2.322e+00	1.000e−23	1.000e+01	1.000e+00	1.501e+01
J055124.27+272301.5	8.317	0.255	3.777e+00	7.043e+03	1.709e−05	4.927e+02	1.220e+00	−9.799e−01	9.738e+00	6.235e−21
	4.927e+02	1.777e+00	4.771e+01	1.831e−22	8.606e+00	8.606e+00	1.000e−23	1.000e+01	1.000e+00	5.674e−01
J055110.28+273154.2	8.449	0.255	2.655e+00	9.242e+03	9.852e−02	2.247e+02	1.071e+00	−9.608e−01	1.277e+00	3.427e−2
	2.247e+02	1.175e+00	1.755e+01	1.802e−22			1.000e−23	1.000e+01	1.000e+00	8.073e+01
J055129.04+272816.8	7.613	0.255	8.326e+00	3.970e+03	1.719e−03	5.571e+01	1.166e+00	−1.419e+00	6.015e+00	1.048e−18
	5.571e+01	1.493e−02	4.787e+01	3.391e−22			1.000e−23	1.000e+01	1.000e+00	6.581e+01

This paper has been typeset from a TeX/LaTeX file prepared by the author.